

1 The application of S isotopes and S/Se ratios in
2 determining ore-forming processes of magmatic Ni-
3 Cu-PGE sulfide deposits:
4 a cautionary case study from the northern Bushveld
5 Complex

6
7 Jennifer W. Smith^{1,2}, David A. Holwell^{1*}, Iain McDonald³ and Adrian J. Boyce⁴

8
9 ¹Department of Geology, University of Leicester, University Road, Leicester, LE1 7RH,
10 UK.

11 ²AMTEL, 100 Collip Circle, Suite 205, University of Western Ontario Research Park,
12 London, Ontario, Canada N6G 4X8

13 ³School of Earth and Ocean Sciences, Cardiff University, Park Place, Cardiff, CF10 3YE,
14 UK.

15 ⁴Scottish Universities Environmental Research Centre, Rankine Avenue, Scottish
16 Enterprise Technology Park, East Kilbride, G75 0QF, UK.

17
18 *Corresponding author details: dah29@le.ac.uk +44(0)1162523804

19
20 Revised version submitted to: Ore Geology Reviews

21

22

23 **Abstract**

24 The application of S/Se ratios and S isotopes in the study of magmatic Ni-Cu-PGE
25 sulfide deposits has long been used to trace the source of S and to constrain the role of
26 crustal contamination in triggering sulfide saturation. However, both S/Se ratios and S
27 isotopes are subject to syn- and post-magmatic processes that may alter their initial
28 signatures. We present *in situ* mineral $\delta^{34}\text{S}$ signatures and S/Se ratios combined with bulk
29 S/Se ratios to investigate and assess their utility in constraining ore-forming processes
30 and the source of S within magmatic sulfide deposits.

31 Magmatic Ni-Cu-PGE sulfide mineralisation in the Grasvalley Norite-Pyroxenite-
32 Anorthosite (GNPA) member, northern Bushveld Complex was used as a case study
33 based on well-defined constraints of sulfide paragenesis and local S isotope signatures. A
34 crustal $\delta^{34}\text{S}$ component is evident in the most primary sulfide assemblage regardless of
35 footwall lithology, and is inferred that the parental magma(s) of the GNPA member was
36 crustally contaminated and sulfide saturated at the time of emplacement. However, S/Se
37 ratios of both the primary and in particular secondary sulfide assemblages record values
38 within or below the mantle range, rather than high crustal S/Se ratios. In addition, there is
39 a wide range of S/Se ratio for each sulfide mineral within individual assemblages that is
40 not necessarily consistent with the bulk ratio. The initial crustal S/Se ratio is interpreted
41 to have been significantly modified by syn-magmatic lowering of S/Se ratio by sulfide
42 dissolution, and post-magmatic lowering of the S/Se ratio from hydrothermal S-loss,
43 which also increases the PGE tenor of the sulfides. Trace element signatures and
44 variations in Th/Yb and Nb/Th ratios support both an early pre-emplacement
45 contamination event as seen by the S isotopes and S/Se ratios, but also a second
46 contamination event resulting from the interaction of the GNPA magma with the local
47 footwall country rocks at the time of emplacement; though this did not add any additional
48 S. We are able to present an integrated emplacement and contamination model for the
49 northern limb of the Bushveld Complex.

50 Although the multitude of processes that affect variations in the $\delta^{34}\text{S}$ signature and in
51 particular S/Se ratio being problematic in interpreting ore genesis, they can reveal a
52 wealth of additional detail on a number of processes involved in the genetic history of a
53 Ni-Cu-PGE deposit in addition to crustal contamination. However, a prerequisite for
54 being able to do this is to utilise other independent petrological and mineralogical

55 techniques that provide constraints on both the timing and effect of various ore-forming
56 and modifying processes. Utilizing both bulk and *in situ* methods in concert to determine
57 the S/Se ratio allows for the assessment of multiple sulfide populations, the partitioning
58 behaviour of Se during sulfide liquid fractionation and also the effects of low temperature
59 fluid alteration. In comparison, S isotopes are relatively more robust and represent a more
60 reliable indicator of the role of crustal S contamination. The addition of trace element
61 data to the above makes for an incredibly powerful approach in assessing the role of
62 crustal contamination in magmatic sulfide systems.

63 **Keywords**

64 Magmatic sulfides; S/Se ratios; S isotopes; Bushveld Complex; GNPA member, Platreef

65

66 1. Introduction

67 Magmatic sulfide deposits of Ni, Cu and platinum-group elements (PGE) form when
68 mafic/ultramafic magmas become saturated in sulfide, and an immiscible sulfide liquid
69 scavenges chalcophile metals from the silicate magma (e.g. Naldrett 2011). Whilst some
70 S is present within such magmas from melting of their mantle sources, many consider the
71 addition of S via assimilation of S-bearing country rocks critical in triggering the
72 generation of large magmatic ore deposits such as Noril'sk and Voisey's Bay (e.g.
73 Grinenko 1985; Leshner and Groves 1986; Leshner and Burnham 2001; Leshner and Keays
74 2002; Li et al. 2002; Lightfoot and Keays 2005). Sulfur/selenium ratios and S isotopes
75 have long been used to investigate the source of S in magmatic sulfide deposits to
76 constrain the role of crustal contamination in ore genesis (e.g. Eckstrand and Cogulu
77 1986; Eckstrand et al. 1989; Peck and Keays 1990; Ripley 1990; Thériault and Barnes
78 1998; Holwell et al. 2007; Ihlenfeld and Keays 2011; Sharman et al. 2013). In addition, a
79 number of trace element ratios and patterns can be used to determine crustal
80 contamination in more broad terms, not specific to addition of S (e.g. Lightfoot and
81 Hawkesworth 1988; Lightfoot et al. 1990).

82 The S/Se ratio of the mantle is well-constrained at 2850–4350 (Eckstrand and Hulbert
83 1987), with average values indicated by McDonough and Sun (1995), Hattori et al.
84 (2002) and Lorand et al. (2003) of 3333, 3300 and 3150, respectively. The mantle values
85 are slightly elevated from chondritic values, reported by Driehus et al. (1995) to be 2500
86 ± 270 in meteorites. The mantle also exhibits a constrained $\delta^{34}\text{S}$ signature of $0 \pm 2\text{‰}$
87 (Ohmoto and Rye 1979). In comparison, crustal rocks may exhibit $\delta^{34}\text{S}$ values in the
88 range of $<-40\text{‰}$ to $>+30\text{‰}$ and mostly have S/Se ratios of 3500 to 100,000 (Yamamoto,
89 1976). Therefore, magmatic Ni-Cu-PGE deposits characterized by S/Se ratios and $\delta^{34}\text{S}$
90 values within or close to the mantle range can be interpreted to have S of mantle origin
91 (e.g. Buchanan et al. 1981; Barnes et al. 2009). In contrast, S/Se ratios exceeding the
92 mantle range or $\delta^{34}\text{S}$ signatures distinct from that of mantle S can be used to signify a
93 substantial contribution of externally derived S (e.g. Thériault and Barnes 1998; Leshner
94 and Burnham 2001; Ihlenfeld and Keays 2011).

95 In recent years, however, it has become apparent that the interpretation of S/Se ratios, and
96 to a lesser extent S isotope signatures, in terms of the input of crustal S, is subject to a
97 number of uncertainties, implemented primarily by the ability of syn- and post-magmatic

98 processes to modify the initial values of both indicators. For S/Se ratios these modifying
99 processes include: variations in the sulfide to silicate ratio (R-factor; Queffurus and
100 Barnes 2015); preferential retention of Se in the mantle during partial melting (Hattori et
101 al. 2002); ‘multistage-dissolution upgrading’ which involves partially dissolving sulfide
102 at depth (e.g. Kerr and Leitch 2005; Holwell et al. 2011; McDonald et al. 2012; Holwell
103 et al. 2014); apparent fractionation of Se between monosulfide solid solution and
104 intermediate solid solution (Helmy et al., 2010); metamorphism (Queffurus and Barnes,
105 2015) and post-magmatic S-loss (Yamamoto 1976; Howard 1997). In addition, a number
106 of processes are known to affect S isotope compositions, including magma degassing,
107 changes in magma redox state, fractionation by crystallization of sulfide at different
108 temperatures (Ohmoto and Rye 1979) and S isotope exchange between the crustally
109 contaminated sulfide liquid and mantle S (Ripley and Li 2003); though these are thought
110 to have a much more restricted modifying effect than those affecting S/Se ratios.

111 Until recently (e.g. Prichard et al. 2013; Dare et al. 2014; Holwell et al. in review), the Se
112 concentration of sulfides could not be determined accurately using *in situ* techniques, and
113 so previous studies utilized S/Se ratios that were representative of bulk rock values (e.g.
114 Ripley 1990; Thériault and Barnes 1998; Ripley et al. 2002; Hinchey and Hattori 2005;
115 Ihlenfeld and Keays 2011; Holwell et al. 2014). In this paper we determine Se contents of
116 sulfides by laser ablation-inductively coupled plasma-mass spectrometry (LA-ICP-MS)
117 in addition to bulk rock concentrations and, for the first time, combine these with a
118 detailed $\delta^{34}\text{S}$ study to establish whether the effects of a variety of processes modify these
119 indicators independently. We also utilise trace element geochemistry as a separate,
120 independent indicator of crustal contamination. Together, these integrated techniques
121 make a powerful approach to the assessment of contamination in the development of
122 magmatic sulfide deposits.

123 We use a magmatic sulfide deposit from the northern limb of the Bushveld Complex; the
124 Grasvalley Norite-Pyroxenite-Anorthosite (GNPA) member, where a number of magmatic
125 and hydrothermal processes are well constrained (Smith et al., 2011; 2014; Maier et al.,
126 2008) as a case study. In doing so, we are able to assess the utility of S/Se ratios and S
127 isotopes on a mineralogical versus bulk rock scale in constraining ore-forming processes.
128 In particular, we show that they can be used to elucidate a number of syn-and post
129 magmatic processes in addition to providing evidence for the source of S. Furthermore,

130 we highlight why an appreciation of these other processes is required to be able to fully
131 apply S/Se ratios and S isotopes to the interpretation of crustal contamination.

132 **2. The S/Se ratios of magmatic sulfides**

133 A number of studies have all constrained the mantle range of S/Se ratios to be close to
134 that defined by Eckstrand and Hulbert (1987) as 2850–4350, with McDonough and Sun
135 (1995), Hattori et al. (2002) and Lorand et al. (2003) all calculating averages around
136 3250. Thus, magmatic sulfides with S/Se ratios within this range can generally be
137 interpreted to have S mostly of mantle origin. Crustal rocks have S/Se ratios higher than
138 the mantle range, <100,000 (Yamamoto 1976), and so contaminated magmatic sulfides
139 will generally show S/Se ratios higher than those of the mantle. Critically, however,
140 initial magmatic S/Se ratios can be modified by a number of processes (Queffurus and
141 Barnes 2015), thus masking or eradicating the evidence traditionally used for interpreting
142 contamination effects. Whilst this makes contamination studies more complex, it
143 illustrates that S/Se ratios can actually be used much wider in the identification of a
144 number of syn- and post-magmatic processes.

145 Due to the chalcophile nature of elements such as Se and PGE, their concentration in
146 sulfide is primarily dependent on the ability of the sulfide liquid to effectively interact
147 with a large volume of silicate magma (i.e. the R-factor). The sulfide/silicate melt
148 partition coefficient ($D_{\text{sul/sil}}$) of the PGE ranges from 17,000 to 92,000 (Naldrett 2011 and
149 references therein) and possibly up to 500,000 for Pd (Mungall and Brenan 2014).
150 Although Patten et al. (2013) report a $D_{\text{sul/sil}}$ value of 323 for Se, it is more generally
151 accepted that the $D_{\text{sul/sil}}$ value applicable to most magmatic sulfide systems is closer to
152 those calculated by Peach et al. (1990) and Brenan (2015) of 1700 and 1388, respectively.
153 Variations in R-factor will also have an effect on the Se concentration of a sulfide and
154 thus also its S/Se ratio (e.g. Thériault and Barnes 1998; Ihlenfeld and Keays 2011). To
155 illustrate, an increase in R-factor will further enrich the sulfide liquid in PGE and Se, thus
156 producing sulfides characterized by very high PGE and relatively high Se tenors and low
157 S/Se ratios (i.e. potentially lower than the mantle range; Queffurus and Barnes 2015).

158 Low S/Se ratios combined with high PGE tenors can also potentially be generated
159 through a process termed ‘multistage-dissolution upgrading’ (Kerr and Leitch 2005)
160 where sulfides may be partially dissolved as multiple batches of S-undersaturated magma
161 interact with sulfide liquid. This process is analogous to an increase in R-factor,

upgrading metal tenors of elements with high sulfide/silicate melt partition coefficients ($D_{\text{sul/sil}}$), including the PGE and Se. Conversely, elements with low partition coefficients such as Fe and S will be preferentially resorbed by the magma thus the highest PGE tenor sulfides will exhibit the lowest S/Se ratios. Consequently, variations in R-factor and sulfide dissolution may mask or reduce an initial crustal or even mantle signature (e.g. Merensky Reef, Naldrett et al. 2009; Platreef, McDonald et al. 2012; River Valley Intrusion, Ontario, Holwell et al. 2014).

In addition, the Se contents of the initial silicate magma may also be modified during crystallization through early extraction of a sulfide liquid from the silicate magma. Due to the relatively high ($D_{\text{sul/sil}}$) of Se, this effectively depletes the remaining silicate magma in Se, increasing the S/Se ratio to crustal-like values in the overlying cumulates (Barnes et al. 2009); analogous to Cu/Pd ratio increases (Maier et al. 1996). Furthermore, due to the apparent preferential retention of Se over S in the mantle the initial Se concentration and thus S/Se values of mantle derived magmas may also vary depending on the degree of partial melting and previous melting history of the mantle source (Hattori et al. 2002; Lorand et al., 2013). Thus magmas derived through re-melting of the mantle are considered capable of producing very low S/Se ratios (<1000) as the magma is depleted in S and enriched in Se (Hattori et al. 2002).

Sulfur/selenium ratios can also be modified further by late stage- to post-magmatic processes including: low temperature hydrothermal alteration; supergene weathering; serpentinization and metamorphism (Queffurus and Barnes 2015). As S is relatively more mobile than Se in hydrothermal fluids below temperatures of around 500°C (Ewers 1977) and is thus preferentially incorporated into aqueous fluids (Yamamoto 1976; Howard 1977), all of these fluid processes can result in preferential S-loss leading to a lowering of S/Se ratios (e.g. Peck and Keays 1990; Cawthorn and Meyer 1993; Maier and Barnes 1996; Ripley et al. 2002; Hinchey and Hattori 2005).

3. The S isotope composition of magmatic sulfides

The $\delta^{34}\text{S}$ signatures of sulfides in a magmatic sulfide deposit should reflect a magmatic, or mantle, signature of 0 ± 2 ‰ if the S in the sulfide is primarily sourced from the magma from which it separated. However, sulfides with $\delta^{34}\text{S}$ compositions that deviate from that of mantle S are often attributed to have incorporated S from a crustal source, with black shales and evaporates among the most common contributors of crustal S (e.g.

194 Ripley et al., 2003; Penniston-Dorland et al. 2012). The role of crustal contamination can,
195 however, only be assessed if the isotopic composition of the country rock S is distinct
196 from that of the local mantle. Since the bacterial processes (biologically mediated
197 reduction of sulfate, e.g. Chambers and Trudinger 1979; Habicht and Canfield 1997)
198 responsible for much of the S isotope fractionation found in sedimentary rocks were not
199 established until around 2.7 Ga, all Archaean rocks older than this contain $\delta^{34}\text{S}$ similar to
200 the mantle range (Grassineau et al. 2005).

201 In addition to the assimilation of S-bearing country rocks, S isotope variations in mafic
202 magmas may also be caused by magma degassing associated with low pressure
203 emplacement, changes in the redox state of the magma, fractionation by crystallization of
204 sulfide at different temperatures (Ohmoto and Rye 1979) and S isotope exchange
205 between the crustally contaminated sulfide liquid and mantle S (Ripley and Li 2003).
206 Whilst the effects of the former three processes on $\delta^{34}\text{S}$ values are considered negligible
207 (up to 1‰ fractionation; Ohmoto and Rye 1979; Miyoshi et al. 1984; Ripley and Li 2003,
208 and references therein), S isotope exchange may be capable of masking or eliminating an
209 initial crustal $\delta^{34}\text{S}$ signature and thus evidence of the earliest stage of ore genesis (e.g.
210 Platreef; Ihlenfeld and Keays 2011). In deposits which have experienced multiple
211 contamination events (pre-, syn- and post- emplacement), the initial isotope composition
212 of the sulfide liquid may also be erased or overprinted by later, localised contamination
213 through the addition of crustal S that is distinct in its isotopic composition (e.g. Platreef;
214 Holwell et al. 2007; Ihlenfeld and Keays 2011; Sharman et al. 2013).

215 **4. The Grasvally Norite-Pyroxenite-Anorthosite member**

216 The 400–800 m thick GNPA member is located in the northern limb of the Bushveld
217 Complex, south of the Ysterberg–Planknek Fault and lies at the equivalent stratigraphic
218 position to the Platreef, being overlain by Main Zone cumulates of the Rustenburg
219 Layered Suite (Fig. 1). It is underlain by Lower Zone cumulates west of the Grasvally
220 Fault and Paleoproterozoic Transvaal Supergroup sediments comprised of the
221 Magaliesberg Quartzite Formation to the east (Fig. 1). The GNPA member comprises
222 vari-textured gabbro-norites, norites, anorthosites, pyroxenites and at least one PGE-
223 bearing chromitite (Hulbert 1983; Smith et al. 2011) and is typically sub-divided into
224 three distinct stratigraphic units (de Klerk 2005): the Lower Mafic Unit (LMF); the
225 Lower Gabbro-norite Unit (LGN); and the Mottled Anorthosite Unit (MANO). The LMF

226 is distinguished from the homogeneous gabbro-norites of the LGN by elevated bulk Cr
227 values. The MANO is recognised by a substantial increase in plagioclase cumulates and
228 the development of lithologies such as mottled and spotted anorthosites (Hulbert 1983;
229 Smith et al. 2011). The LGN, which is completely barren of PGE-bearing sulfides, is
230 thought to represent a sill of Main Zone rocks (de Klerk 2005). Detailed descriptions on
231 the geology of the succession and associated PGE and BMS mineralization are provided
232 in Hulbert (1983), McDonald et al. (2005), Maier et al. (2008) and Smith et al. (2011,
233 2014).

234 *4.1. Sulfide mineralogy*

235 The observed distribution and mineralogy of sulfides and PGE results from processes of
236 both magmatic sulfide fractionation and low temperature (<230°C) fluid alteration (Fig.
237 2; Smith et al. 2011; 2014). In places, a primary pyrrhotite–pentlandite–chalcopyrite
238 sulfide assemblage (Fig. 2A) has been replaced to varying extents by a low temperature
239 assemblage of pyrite, millerite and chalcopyrite (Fig. 2B and C). The degree of
240 replacement varies significantly throughout the succession and can be viewed as a
241 continuum from a purely magmatic sulfide assemblage to almost completely replaced
242 sulfides (Fig. 2; Smith et al. 2011). Remobilization and redistribution of PGE is limited,
243 with some platinum-group minerals (PGM) recrystallization *in situ* and pyrite and
244 millerite inheriting PGE contents of the phases replaced (Fig. 2; Smith et al. 2014). The
245 underlying Magaliesberg Quartzites contain some sedimentary pyrite, which is texturally
246 distinct from the sulfide of magmatic assemblage that has infiltrated the floor rocks
247 (Smith et al., 2011).

248 *4.2. Justification as a case study*

249 The GNPA member represents a favourable case study for several reasons. Firstly, the
250 sulfide mineralization has been studied in detail, in terms of mineralogy, distribution and
251 hydrothermal interaction (Smith et al. 2011, 2014), enabling the effects of secondary
252 alteration to be easily identified and thus considered in any interpretation. The well-
253 defined primary sulfide assemblage and low temperature hydrothermal overprint provide
254 the opportunity to assess in detail the partitioning behaviour of Se during sulfide
255 fractionation *and* its mobility during low temperature alteration.

256 Secondly, the isotopic composition of the local mantle and crustal rocks are well
257 constrained providing reliable end members. The S isotope signature of the mantle
258 immediately beneath the northern Bushveld Complex can be considered to be represented
259 by sulfide inclusions in diamonds within the Klipspringer kimberlite, 25 km east of
260 Mokopane, which exhibit $\delta^{34}\text{S}$ values of -1.8 to +2.4‰, with a mean of +1.0‰
261 (Westerlund et al. 2004). Previous studies into the isotopic composition of the Transvaal
262 Supergroup have revealed that sulfide-bearing shales from the Duitschland Formation
263 and Timeball Hill Formation have $\delta^{34}\text{S}$ signatures ranging from -18‰ to +10‰
264 (Cameron 1982; Sharman-Harris et al. 2005; Sharman et al. 2013). Sulfides within the
265 Duitschland Formation and Malmani Subgroup are isotopically distinct with $\delta^{34}\text{S}$
266 signatures ranging from +10‰ to >+30‰ (Sharman et al. 2013). Additionally, the
267 abundance of S isotope data available for the adjacent Platreef (Manyeruke et al. 2005;
268 Sharman-Harris et al. 2005; Holwell et al. 2007; Penniston-Dorland et al. 2008) enables a
269 direct comparison of the GNPA member with its nearest analogue. Penniston-Dorland et
270 al. (2012) report $\delta^{34}\text{S}$ values for the Merensky Reef and UG2 deposits of $2.2 \pm 0.6\text{‰}$.

271 There is also S/Se data for other PGE deposits in the Bushveld Complex. Naldrett et al.
272 (2009) report a ‘magmatic’ S/Se ratio of 2080 for the Merensky Reef, which is lower than
273 the mantle range, though the authors invoke a staging chamber model whereby sulfides
274 partially dissolve prior to emplacement. This would lower the S/Se ratio as explained
275 above by increasing the Se tenor. As such, we do not consider this ‘magmatic’ range to
276 be representative of the local mantle S/Se signature, but more specific to the Merensky
277 Reef and the processes involved in its formation. In the northern limb, Ihlenfeld and
278 Keays (2011) report a range of S/Se ratios from 1500 to 13,000 for the Platreef which
279 show clear crustal input, but a range of values that extend well below that of the mantle
280 range. McDonald et al. (2012) report S/Se ratios from homogenised sulfide melt
281 inclusions in the Platreef between 400 and 7000, with most in the range 1000-2000.
282 Similarly, this was explained by a process of sulfide dissolution and metal upgrading at
283 depth.

284 Thirdly, as the GNPA member is underlain by both Lower Zone cumulates and basement
285 metasedimentary rocks the effect, if any, of localised contamination and the *in situ*
286 assimilation of country rocks along strike should be easily recognized along with any
287 related overprinting signatures.

288 **5. Samples and Methods**

289 Samples of quarter core were obtained from nine boreholes drilled by Falconbridge Ltd
290 and Caledonia Mining on the farms Rooipoort, Grasvally, Moorddrift and War Springs
291 (Fig. 1). The sample suite covers a full range of GNPA member lithological units and
292 mineralized zones, including areas identified by Smith et al. (2011; 2014) that have
293 experienced fluid interaction, and cover a strike length of around 15 km (Fig. 1) that
294 covers footwall consisting of Lower Zone harzburgites, and the Magaliesberg Quartzite
295 Formation (Fig. 1).

296 The majority of the S isotope data was determined utilizing the *in situ* laser ablation
297 technique at SUERC within the NERC funded Isotope Community Support Facility
298 (Table 1). This method was favoured over conventional analyses as textural
299 inhomogeneities are easily identifiable, thus enabling the analysis of individual minerals
300 within textually complex multi-phase sulfide aggregates. In addition it also allows
301 analysis of sulfides that would be considered too small for conventional analysis.
302 Polished blocks of 45 samples were placed into a sample chamber, which was evacuated
303 and subsequently filled with an excess of oxygen gas. Sample areas, previously selected
304 using reflected-light microscopy, were combusted using a SPECTRON LASERS 902Q
305 CW Nd-YAG laser (1-W power), operating in TEM00 mode. Details of the system
306 design, laser characteristics and experimental conditions are described in Kelley and
307 Fallick (1990) and Wagner et al. (2002). The SO₂ gas produced by each laser combustion
308 was cryogenically purified in a miniaturized glass extraction line using a CO₂/acetone
309 slush trap to remove water and a standard n-pentane trap to separate SO₂ from trace CO₂.
310 During the laser ablation technique there is a systematic fractionation of $\delta^{34}\text{S}$ values of
311 the resulting SO₂ gas compared to the mineral $\delta^{34}\text{S}$ (Wagner et al. 2002). The
312 fractionation factors used to correct the data are established for the SUERC facility and
313 are as follows: pyrrhotite +0.4, pentlandite +1.9, chalcopyrite +0.7, pyrite +0.8 and
314 millerite +1.9‰. Repeated analysis of individual sulfide phases revealed in general a
315 reproducibility of $\pm 0.2\%$. Larger discrepancies (up to $\pm 1\%$) however do exist between
316 and within individual pyrite grains, revealing small-scale heterogeneity. All $\delta^{34}\text{S}$ values
317 were calculated relative to the Vienna-Canon-Diablo Troilite (V-CDT) standard and are
318 reported in standard notation.

319 Several sulfide samples which exhibited textural and compositional homogeneity in
320 reflected-light were selected for conventional analysis (Table 1). Individual sulfide
321 phases were micro-drilled from nine polished blocks. Each analysis used 4-5 mg of
322 sulfide which was subsequently converted to SO₂ for mass spectrometric analysis by
323 combustion with 0.2 g of cuprous oxide, following the procedure of Robinson and
324 Kusakabe (1975). Samples were combusted under vacuum at 1,070°C for 25 minutes and
325 the SO₂ gas produced was purified prior to analysis in a VG SIRA II gas mass
326 spectrometer in a glass extraction line analogous to that used for laser analysis. Raw
327 instrument $\delta^{66}\text{SO}_2$ data were converted to $\delta^{34}\text{S}$ values by calibration with international
328 standards NBS-123 (+17.1‰) and AEA-S-3 (−31.5‰), as well as SUERC's internal lab
329 standard CP-1 (−4.6‰).

330 Subsequent to $\delta^{34}\text{S}$ analysis, Se concentrations of sulfides were determined *in-situ* by
331 Laser Ablation-ICP-MS using a New Wave Research UP213 UV laser system coupled to
332 a Thermo X Series 2 ICP-MS at Cardiff University. The relative abundances of PGE and
333 other elements were recorded in time-resolved analyses mode (time slices of 250 ms) as
334 the laser beam followed a line designed to sample different sulfide or oxide phases. The
335 beam diameter employed was 30 μm , with a frequency of 10 Hz and a power of $\sim 6 \text{ J cm}^{-2}$.
336 The sample was moved at 6 $\mu\text{m sec}^{-1}$ relative to the laser along a pre-determined line
337 pattern. Ablations were carried out under helium (flow $\sim 0.7 \text{ L min}^{-1}$) and the resulting
338 vapour combined with argon (flow rate 0.65-0.75 L min^{-1}) before delivery to the ICP-MS.
339 Acquisitions lasted between 80 and 400 seconds, including a 20 second gas blank prior to
340 the start of the analysis and a 10 second washout at the end. Counting errors averaged at
341 12% and 19% for standards containing 108 ppm Se and 57 ppm Se, respectively.

342 The S content of sulfides analysed was obtained from a JEOL JXA-8600S electron
343 microprobe at the University of Leicester using an accelerating voltage of 15 kV and a
344 probe current of 30 nA with a focussed beam of <0.5 microns. Sulfur was used as internal
345 standard for the LA work. Subtraction of gas blanks and internal standard corrections
346 were performed using Thermo Plasmalab software. Calibration was performed using a
347 series of 5 synthetic Ni-Fe-S standards prepared from quenched sulfides. The standards
348 incorporate S, Ni, Fe and Cu as major elements and Co, Zn, As, Se, Ru, Rh, Pd, Ag, Cd,
349 Sb, Te, Re, Os, Ir, Pt, Au and Bi as trace elements and the compositions of the 5
350 standards are given in Prichard et al (2013)

351 In order to directly compare *in-situ* S isotopes with *in-situ* S/Se ratios, Se concentrations,
352 where possible, were obtained from the same grains as the $\delta^{34}\text{S}$ analysis. In samples
353 where the $\delta^{34}\text{S}$ analysis resulted in combustion of the entire grain, Se was determined for
354 adjacent grains. In the majority of samples *in situ* S/Se ratios utilize an average S content
355 of either chalcopyrite, pyrite, pentlandite, pyrrhotite or millerite which were determined
356 by electron microprobe analysis prior to LA-ICP-MS (see Appendix 2). In samples where
357 microprobe data was not available stoichiometric values of S were used.

358 Bulk rock S was determined by standard combustion procedures using a Laboratory
359 Equipment Company C2320 (LECO) titrator at the University of Leicester. In total 23
360 samples were submitted to ALS Global Laboratories, Ireland, for determination of whole
361 rock Se using Aqua Regia digest followed by ICP-MS and ICP-AES.

362 To recalculate whole rock Pt and Pd contents in 100% sulfide the formula provided by
363 Barnes and Lightfoot (2005) was used:

$$364 \quad C_{(100\%sul)} = C_{wr} \times 100 / (2.527 \times S + 0.3408 \times Cu + 0.4715 \times Ni)$$

365 Where $C_{(100\%sul)}$ is the concentration of Pd or Pt in 100 % sulfide, C_{wr} is the concentration
366 of the element in whole rock and S , Cu and Ni is the concentration in wt % of these
367 elements in whole rock.

368 A suite of 48 samples of crushed quarter core, representative of the main stratigraphic
369 units of the GNPA member (LMF: 15 samples, LGN: 13 samples and MANO: 20
370 samples) and the local metasediments (4 samples), were analysed for bulk rock
371 geochemistry as a further indicator of crustal contamination. Major elements were
372 determined by X-ray Fluorescence at the University of Leicester on fusion beads
373 produced by mixing milled powders (ignited to 950°C to determine loss on ignition) with
374 Johnson-Matthey spectroflux JM100B (80% Lithium Metaborate, 20% Lithium
375 Tetraborate) and then fired in a platinum crucible. Trace elements were determined at
376 Cardiff University using a JY Horiba Ultima 2 inductively coupled plasma optical
377 emission spectrometer (ICP-OES) and Thermo X7 series inductively coupled plasma
378 mass spectrometer (ICP-MS). Ignited powders were fused with Li metaborate on a
379 Claisse Fluxy automated fusion system to produce a melt that could be dissolved in 2%
380 HNO_3 for analysis. Full details of the standard ICP analysis procedures and the

instrumental parameters are given in McDonald and Viljoen (2006). Full geochemical data for the suite of samples analysed is given in Table A1.

6. Sulfur isotopes

The results of more than 130 analyses of sulfides from the GNPA member and associated country rocks are provided in Table 1 and Figure 2; representing the most comprehensive S isotope study to date on the southernmost sector of the northern limb of the Bushveld Complex. With the exception of the chomitites, the primary and secondary sulfide assemblages are very similar, overlapping the boundary of mantle and crustal values. Our results are in agreement with the limited (n=16) $\delta^{34}\text{S}$ data previously presented by Maier et al. (2008) on the GNPA member which ranges from $\delta^{34}\text{S}$ +1.8‰ to +5.1‰ with a mean of +3.7‰. However, this study did not discriminate between the two important textural and paragenetic generations of sulfide, as our study does.

6.1. Non chromitiferous rocks

6.1.1. Primary sulfide assemblages

The pyrrhotite-pentlandite-chalcopyrite assemblage has a $\delta^{34}\text{S}$ range of +1.6 to +4‰ with a mean of +2.8‰. Table 1 indicates there is no systematic change with stratigraphic height in any of the drillholes sampled. The majority of analyses reveal signatures indicative of some crustally derived S, with only five analyses, all of which were of pyrrhotite, residing within the local mantle range of -1.8 to +2.4‰ (Table 1). Even where the basal LMF unit is directly underlain by Lower Zone cumulates rather than metasediments of the Transvaal Supergroup, all of the primary sulfides analysed reveal crustal $\delta^{34}\text{S}$ signatures (Fig. 3A; Table 1).

6.1.2. Secondary sulfide assemblages

The $\delta^{34}\text{S}$ signatures of 59 analyses of secondary sulfides range from +0.9 to +6.8‰ (mean of +3.5‰; less than 1 ‰ higher than the mean of the primary sulfides). A crustal S component is evident within the majority of the early pyrrhotite, chalcopyrite and pentlandite although some relicts of primary pyrrhotite and chalcopyrite exhibit $\delta^{34}\text{S}$ values consistent with local mantle S, but these make up just ten (17%) of the analyses (Table 1). The late pyrite and millerite have $\delta^{34}\text{S}$ signatures ranging from +2.6 to +6.8‰ (Fig. 3B). Sulfide phases within each sample are fairly consistent in terms of their isotopic composition, with up to 2‰ variation observed (Table 1). There is no evidence

of a stratigraphic or lateral control over the distribution/preservation of the mantle like signatures as they are distributed throughout the GNPA member irrespective of a Lower Zone cumulates or quartzite footwall.

6.2. *Chromitiferous rocks*

Throughout the GNPA, the chromitites in the LMF are isotopically distinct from the rest of the GNPA member, with $\delta^{34}\text{S}$ values consistently 1 to 2 ‰ heavier than the primary and secondary sulfide assemblages (see Fig. 3C), ranging from +2.8 to +7.1 ‰ with a mean of +5.4 ‰ (Table 1; Fig. 3C).

6.3. *Country rocks*

Sulfides within the quartzite footwall, interpreted to have resulted from infiltration of the magmatic sulfide liquid into the footwall (Smith et al. 2011) and are thus fundamentally magmatic, are isotopically similar to those developed within the GNPA member, exhibiting a range from $\delta^{34}\text{S}$ +3.6 to +5.6 ‰ (Table 1; chalcopryrite and millerite, Fig. 3D). Conversely, metasedimentary pyrite hosted within the Magaliesberg Quartzite Formation displays greater variation in $\delta^{34}\text{S}$ signatures and a very strong crustal component with values ranging from $\delta^{34}\text{S}$ +3.5 to +10.5 ‰ (Table 1; basement pyrite, Fig. 3D).

7. Bulk rock S/Se ratios

Rocks with visible sulfide mineralisation in the GNPA member typically contain 0.1 to 2 wt % S and Se concentrations of <0.2 (detection limit) to 6.1 ppm (Table 2). Due to the highly compatible nature of Se in sulfide a strong positive correlation exists between S and Se throughout the succession (Fig. 4A). Sulfur/selenium ratios are variable from 1495 to 6765, with the majority of samples residing within or below the mantle range of Eckstrand and Hulbert (1987; Table 2; Fig. 4A). However, a few samples exhibited ratios that exceed that of the mantle (Fig. 4A; Table 1), thus being consistent with a crustal source of at least some of their S. All these are from samples from the LMF unit, most of which were obtained west of the Grasvally Fault where Lower Zone cumulates underlie the GNPA member (Table 2). The footwall quartzite samples straddle the upper boundary of the mantle range, however, these samples contain both metasedimentary pyrite and also some magmatically-derived sulfide and so represent a mixed signature.

From the broad negative correlation observed between PGE tenor (defined by Pt+Pt in 100% sulfide) and S/Se ratio, primary and secondary sulfides can be distinguished (Fig. 4B). The former are, in general, characterized by relatively low PGE tenors (typically between 6-<60 ppm, with the exception of the chromitite; Table 2), and S/Se ratios within or above the mantle range (3500-6500; Table 2). In comparison, secondary sulfides are characterized by notably lower S/Se ratios from 1495 to 4210 with only two samples residing within the crustal field, and generally higher PGE tenors (40 to <160 ppm Fig. 4B; Table 2). Figure 4B illustrates clearly that as the S/Se ratio decreases, the PGE tenor progressively increases, signifying either S-loss or addition of Se and PGE. The Se content throughout the GNPA member increases relative to bulk PGE content (Table 2), indicating that both are controlled relatively analogously by the presence of sulfide. A strong correlation also exists between PGE tenor and Se tenor throughout primary and secondary sulfides (Fig. 5).

8. Mineral-scale S/Se ratios

8.1. The Se content of sulfide minerals

The Se contents of pyrrhotite, chalcopyrite, pentlandite, millerite and pyrite typically varies from the detection limit of 60 ppm up to 170 ppm (Table 3). Within the chromitites, concentrations of Se are noticeably elevated with pentlandite and millerite containing up to 220 ppm and 600 ppm, respectively. Representative time resolved analysis (TRA) spectra for the major sulfide phases analysed are provided in Figure 6. Although the Se content of the individual sulfide phases varies slightly between samples, Se appears to be distributed uniformly within each sulfide phase, as shown by the smooth profiles on the TRA spectra that mirror S (Fig. 6). This clear relationship along the laser lines, plus multiple analyses from single grains indicates a precision within 10%. Whilst all the magmatic sulfide phases contain detectable concentrations of Se in solid solution (Fig. 6A-G), the Se contents of metasedimentary pyrite in the local footwall is noticeably lower at <68 ppm (Fig. 6H).

8.2. The S/Se ratios of sulfide minerals

The S/Se ratio of sulfides was calculated using Se concentrations from LA-ICP-MS analysis and S contents determined by electron microprobe. The S values represent averages of the sulfide phase in each sample. Where microprobe data was not available,

stoichiometric S values were utilized. The results are shown in Figure 7. Sulfur/selenium ratios in the primary chalcopyrite, pyrrhotite and pentlandite vary from 2032 to 5726 (Fig. 7A). Mantle-like S/Se ratios are widespread and are observed in all sulfide phases. Only a few pyrrhotite analyses from west of the Grasvally Fault exhibit S/Se ratios below mantle.

In the secondary assemblages, any relicts of primary pyrrhotite, chalcopyrite and pentlandite show a range in ratios of 2035 to 5917; almost identical to the primary sulfide assemblages although most occurrences fall within the range of 2035 to 3695, which includes a significant proportion of pentlandite displaying S/Se ratios lower than mantle (Fig. 7B; Table 1). Secondary pyrite and millerite, including those within the chromitites are characterised by more variable S/Se ratios which fall within the range of 1975 to 8980 (Table 1). Pyrite from the quartzite footwall exhibits unequivocally crustal S/Se ratios in the crustal range of 5943–8455 (Fig. 7B; Table 1).

9. Trace element indicators of crustal contamination

Whilst S isotopes and S/Se ratios are used to determine crustal contamination specifically involving the addition of S, a number of trace element ratios can reveal more general crustal contamination signatures. Therefore, we also include an analysis of trace element data to further investigate the role of contamination, and independently test the apparent contamination signatures shown by the S/Se ratios and S isotopes. Chondrite-normalized rare earth element (REE) patterns for the GNPA member and its local footwall are provided in Figure 8A-F, with the data included as Table A1. Overall the LMF, LGN and MANO units are characterised by: (i) relatively fractionated REE patterns (La/Lu_n 1.6–14), enriched in the light rare earth elements (LREE); (ii) almost no fractionation of the HREE (Tb/Yb_n 1.1); and (iii) a mostly positive Eu anomaly (Eu/Eu^* 0.8–3.6). The most fractionated profiles (La/Lu_n 5–12) within the GNPA member are associated with samples obtained from the MANO and LMF units overlying metasediments (Fig. 8A,B). Here the rocks show strong enrichment in LREE (Ce/Sm_n 2.1–3.6) and almost no fractionation of the HREE ($\text{Tb/Yb}_n \sim 1$).

It is worth noting that the individual profiles of samples from borehole RP05.45 do not necessarily become progressively enriched in REE with depth (Table A1) and thus proximity to the quartzite footwall. However, LREE concentrations are noticeably

505 elevated within the LMF unit that overlies quartzite (Fig. 8B, c.f. Fig. 8D), indicating
506 some localised contamination over the quartzites. The quartzites themselves exhibit
507 highly fractionated REE patterns (La/Lu_n 11–19) that are significantly more enriched than
508 those of the GNPA lithologies (Fig. 8F).

509 In contrast, where Lower zone cumulates underlie the GNPA member, REE
510 concentrations are comparable between the LMF and MANO units (Fig. 8D,E). Here,
511 REE profiles are fractionated and LREE enriched but less so than observed where the
512 floor is quartzite. Most LMF samples show lower La/Lu_n (1.6–4.8) and Ce/Sm_n (1.3–2)
513 ratios. The LGN unit is notably homogeneous in its REE contents and geochemistry in
514 comparison to the overlying MANO unit and underlying LMF unit, (Fig. 8C) and are
515 consistent with Main Zone data from the Western Bushveld (Maier and Barnes 1998),
516 and the interpretation this is a sill of Main Zone (de Klerk 2005; Maier et al. 2008; Smith
517 et al. 2014).

518 Primitive mantle-normalized, multi-element spider diagrams of representative samples
519 from the GNPA member and its local quartzite footwall are presented in Figure 9.
520 Throughout the succession, trace element signatures are consistent and characterised by
521 pronounced negative Nb, Sr and Ti anomalies and strong enrichment in LILE; all strong
522 indicators of crustal contamination. Whilst the MANO and LMF units exhibit variations
523 in absolute trace element concentrations (Fig 9A,C), the LGN unit exhibits an extremely
524 restricted range in its trace element content and geochemistry (Fig. 9B).

525 The majority of GNPA samples exhibit low $(\text{Nb/Th})_{\text{PM}}$ ratios (< 0.4) and elevated
526 $(\text{Th/Yb})_{\text{PM}}$ ratios (1–24), thus defining a relatively tight trend (very similar to that
527 observed in the Platreef; Ihlenfeld and Keays 2011) on the $(\text{Nb/Th})_{\text{PM}}$ vs. $(\text{Th/Yb})_{\text{PM}}$ plot
528 in Figure 9. With $(\text{Nb/Th})_{\text{PM}}$ ratios < 1 and $(\text{Th/Yb})_{\text{PM}}$ ratios > 5 considered indicative of a
529 crustally contaminated mantle derived magma (Lightfoot and Hawkesworth 1988;
530 Lightfoot et al. 1990; Ihlenfeld and Keays 2011), a crustal influence is noticeable
531 throughout the GNPA member with only a few samples residing within the purely
532 magmatic range (Fig. 10). From the data shown in Figure 9 and 10 however, it is evident
533 that the degree of contamination is not a function of proximity to local footwall
534 metasediments as the basal LMF unit exhibits a similar range in $(\text{Nb/Th})_{\text{PM}}$ and
535 $(\text{Th/Yb})_{\text{PM}}$ ratios to the LGN and MANO units, with this data indicating a signature of

536 bulk contamination of the entire package, and the REE data showing evidence of some
537 localised contamination in addition.

538 **10. Discussion**

539 *10.1. Comparison of S isotopes and S/Se ratios*

540 Figure 11 compares the S isotope data with the bulk rock S/Se data and illustrates that for
541 individual samples, the $\delta^{34}\text{S}$ signatures are rarely in agreement with the S/Se ratios in
542 terms of mantle versus crustal signatures. The notable lack of relationship between bulk
543 rock S/Se ratios and S isotopes within the GNPA member is particularly apparent within
544 the chromitites, which exhibit the most crustal $\delta^{34}\text{S}$ signatures but are characterized by
545 consistently mantle-like S/Se ratios (Fig. 11). This clearly shows that a simple assessment
546 of either of these alone cannot be used with confidence to interpret the source of S
547 unambiguously.

548 One particularly interesting relationship our data show is that during secondary alteration,
549 there is a trend for S/Se ratios to lower to mantle values or below, whereas S isotope
550 values rise to more crustal values (Figs. 3,11). This apparent paradox illustrates the
551 inherent problem in using these ratios as purely crustal contamination indicators. The
552 overall shift of just under 1 ‰ in $\delta^{34}\text{S}$ signatures to heavier values in the secondary
553 sulfide assemblages could very easily be explained by the addition of crustal S during
554 secondary alteration. However, this should also increase the S/Se ratio, which it does not.
555 In fact, the reduction in S/Se ratio in the secondary assemblages is more indicative of S
556 loss, rather than gain, which is highly likely a consequence of the secondary sulfide
557 alteration. The increase in PGE tenor along with the reduction in S/Se (increase in Se
558 tenor; Fig. 4) supports this. Given the mineralogical and geochemical work of Smith et al.
559 (2011; 2014), it is unlikely the secondary alteration introduced any further PGE, and so
560 the increase in tenor during alteration is most likely due to S-loss. Naldrett et al. (2009)
561 also note high PGE tenors and a very consistent, low S/Se ratio of 2080 in the Merensky
562 Reef. They interpret the high tenors to be due to sulfide dissolution in a staging chamber,
563 and whilst this is a different process to the low temperature alteration, the result of losing
564 S relative to Se and PGE is the same.

565 As such, our work this shows how secondary processes can mask the crustal signatures in
566 S/Se ratios. Whilst it is possible that crustal S was added during this process to raise the S

isotope signatures, there would still have to be a large net S loss. What is more likely is that this small shift in S isotope compositions is a result of this alteration. Crystallization of pyrite at low temperatures (<250°C) fractionates $\delta^{34}\text{S}$ by around +1.5 ‰ (Ohmoto and Rye 1979), which would explain perfectly how the pyrite-dominant secondary sulfide assemblage appears around 1 ‰ heavier than the primary assemblages, without the need to add S in the process.

10.2. Comparison of bulk and mineral S/Se ratios

Figure 12 compares the bulk rock S/Se ratios to those of individual sulfide minerals within each sample. The *in situ* S/Se ratios show a very high variability and complexity in comparison to bulk rock ratios (Fig. 12), and in some cases, all our individual analyses sit below or above the bulk rock value, showing that they cannot be fully representative of the overall sulfide population within the sample. This may reflect that in 3D, there are more than one type of sulfide assemblage (primary v secondary) than exposed in the surface of a 2D section. For example, the bulk rock S/Se value for the basement quartzite sample (RP05.45/214) sits within the mantle range. However, the rock is known to contain sulfides of two different generations: sulfides that have infiltrated the floor from the GNPA member, such as pentlandite, have low S/Se ratios; whereas the metasedimentary pyrites have high S/Se ratios around 7000-9000 (Fig 12B). This illustrates the benefit of utilising *in situ* over bulk S/Se analyses in cases where more than one distinct paragenetically defined sulfide assemblage is present. Other disparities however, are less easily explained (e.g. RP04.23/392) and may indicate variability beyond the representativeness of the number of analyses we performed. Either way, it indicates the greater complexity of individual mineral S/Se systematics.

While the isotopic composition of coexisting pyrrhotite, pentlandite and chalcopyrite in the primary sulfides is rather consistent (Fig. 3), the S/Se ratios show greater variability both between and within the individual sulfide phases (Fig. 12A; Table 1). Furthermore, the secondary sulfides have S/Se ratios even more variable than the primary sulfides (Fig. 12B). The range in S/Se ratios is a true reflection on the variable Se contents of the pyrite, which is attributed to the extent to which the primary sulfide phases have been replaced and the ability of pyrite to inherit their Se contents. Thus it is unlikely these variations reflect simply the source of S and thus mineral-scale S/Se ratios have limited use as a reliable indicator of crustal S contribution. However, such variations must be controlled

599 by other processes, and as such, S/Se ratios on this scale can be useful for tracing other
600 ore forming processes.

601 Given the higher variability in S/Se ratio compared to the S isotopes, is it likely that S/Se
602 ratios are more sensitive to other processes and therefore as a simple indicator of crustal
603 contamination, we suggest S isotopes are more reliable. However, that is not to preclude
604 the application of S/Se ratios to studies of crustal contamination, though it does require
605 careful assessment of the rocks to identify any processes that may have been present that
606 could alter an initial S/Se ratio *prior* to interpretation for S source. Contrary to this being
607 problematic, it actually illustrates that S/Se ratios can be used to interpret a number of
608 different syn- and post-magmatic processes *in addition* to crustal contamination.

609 With the well-defined primary sulfide assemblage and a low-temperature hydrothermal
610 sulfide overprint, the GNPA member rocks provide an excellent opportunity to
611 investigate two of these additional processes: (1) the partitioning behaviour of Se during
612 magmatic sulfide fractionation processes and (2) during low temperature fluid alteration
613 (<230°C; Smith et al., 2011) which has not been previously attempted. Below, these are
614 discussed prior to the process of crustal contamination, as interpretation of the latter
615 requires a full appreciation of the effects of the former two.

616 *10.3. Distribution and partitioning of Se in primary sulfide*

617 Since there is greater analytical error associated with Se concentrations that are close to
618 the detection limit of 60 ppm, in the following sections, values <80 ppm have been
619 excluded when considering the partitioning behaviour of Se. The appreciable (80–164
620 ppm) and broadly comparable concentrations of Se in solid solution within coexisting
621 primary pyrrhotite, pentlandite and chalcopyrite (average $\text{Se}_{(\text{po})}/\text{Se}_{(\text{pn})}$, $\text{Se}_{(\text{po})}/\text{Se}_{(\text{cpy})}$ and
622 $\text{Se}_{(\text{pn})}/\text{Se}_{(\text{cpy})}$ ratios of 0.8 to 1.3; Table 3), indicates that Se partitions readily into each
623 magmatic sulfide phase. Thus, Se is likely to be compatible within both high temperature
624 monosulfide solid solution (mss) and intermediate solid solution (iss) and is not
625 significantly partitioned by the lower temperature recrystallization of mss and iss to
626 pyrrhotite-pentlandite-chalcopyrite.

627 The highest concentrations of Se are typically in either pyrrhotite or pentlandite, which
628 contain near comparable Se contents (Table 3). From this, it can be suggested that Se is
629 compatible in mss and during low temperature (<650°C) recrystallization, it partitions

equally into pyrrhotite or pentlandite. Pentlandite and pyrrhotite contain either comparable or slightly higher concentrations of Se to the coexisting Cu-sulfide. Thus, this may indicate evidence for slight preferential partitioning of Se into mss over iss. These features are not specific to the GNPA member or the Bushveld Complex, as LA-ICP-MS data available from the Jinchuan intrusion, China (Prichard et al., 2013), reveal comparable quantities of Se in solid solution within chalcopyrite (mean 133 ppm; n=13), pyrrhotite (mean 151 ppm; n=13) and pentlandite (mean 154 ppm; n=13) with very similar average ratios of $Se_{(po)}/Se_{(pn)}$, $Se_{(po)}/Se_{(cpy)}$ and $Se_{(pn)}/Se_{(cpy)}$ of 0.98, 1.13, 1.15, respectively.

In contrast, experimental work by Helmy et al. (2010) constrained a $D_{Se}^{mss/sul}$ value of 0.6 ± 0.05 , indicating Se preferentially fractionates into the residual Cu-rich sulfide liquid. This is consistent with differences observed in the Se concentration (and S/Se ratio) between the iss and mss fractions within a number of magmatic massive sulfide deposits such as Voisey's Bay, Sudbury and Noril'sk reported by Queffurus and Barnes (2015). The apparent disparities between the observations from these massive sulfides and the disseminated ores of Prichard et al. (2013) and this study may relate to different magmatic sulfide deposit types. Consequently, S/Se ratios provide insights into Se partitioning during sulfide liquid fractionation, and these effects must be considered prior to interpretation of them as a proxy for the source of S.

10.4. Mobility of Se during fluid alteration

Secondary pyrite and millerite were found to also host significant concentrations of Se in solid solution (Table 3) and $Se_{(py)}/Se_{(mil)}$ ratios vary slightly from 1.1 to 1.3 (Table 3). Concentrations of Se in pyrite appear broadly comparable or marginally elevated to the pyrrhotite it has replaced (Table 3), and it largely remains uniformly distributed throughout the primary relicts (Fig. 6E,F) at comparable concentrations to the completely unaltered samples (Fig. 6A-D). The Se concentrations in millerite are more variable, but are generally higher than the pentlandite it replaces (Table 3). As such, the secondary alteration appears to enrich the Se content of the secondary sulfides, consistent with the earlier discussion of there being a net S loss during the alteration process, which also increases the PGE tenor. This is consistent with the metasedimentary pyrite containing very low Se contents compared with pyrite formed from alteration of Se-rich magmatic pyrrhotite.

662 The presence of this secondary sulfide assemblage in the GNPA member provides an
663 opportunity to explore the behaviour of Se during low temperature alteration. Similar low
664 temperature assemblages have been recognised in a number of magmatic sulfide deposits
665 (Dare et al., 2011; Djon and Barnes 2012; Piña et al. 2012). From our data it appears that
666 Se is relatively immobile and remains within the sulfide, being taken up by both pyrite
667 and millerite. Furthermore, the increase in Se tenor and reduction in S/Se ratio is
668 consistent with there being bulk S loss during the alteration, indicating preferential S
669 mobility. The lack of PGE mobilisation (Smith et al. 2014) also shows that PGE are
670 relatively immobile alongside Se under these conditions. Whilst this attests to the
671 immobility of PGE and Se during low temperature alteration of this kind, Prichard et al.
672 (2013) have shown that Se can behave in a mobile manner, but only within saline, low
673 pH, highly oxidizing fluids. The highly oxidising conditions required to remobilise Se in
674 low temperature fluids (100–300°C) are indicated in the Jinchuan intrusion by the
675 unusual association of Se-bearing PGM with a magnetite–hematite alteration assemblage.
676 The GNPA member and Platreef lack evidence of such assemblages and thus we infer
677 that the fluid composition affecting the GNPA member were not suitable for
678 remobilisation of Se or PGE, but were responsible for the alteration of the sulfide
679 assemblage.

680 Therefore, within most magmatic ore deposits, low temperature hydrothermal alteration
681 that preferentially removes S over Se and PGE will act to increase the tenors of the
682 sulfides in the secondary assemblages, with a concurrent *reduction* in S/Se. Therefore, it
683 is essential to identify if any secondary hydrothermal activity has affected the S and Se
684 contents before S/Se ratios are used to interpret the source of S. Furthermore, S/Se
685 systematics can be used additionally to investigate S and Se mobility during low
686 temperature alteration, alongside careful paragenetic studies.

687 *10.5. Crustal contamination and the source of S in the GNPA member*

688 The above discussion demonstrates that where syn and/or post magmatic processes have
689 significantly altered the initial composition of a sulfide liquid or sub-solidus assemblage,
690 S/Se ratios need to be applied in conjunction with S isotopes and robust mineralogical
691 understanding to confidently assess the role of contamination in ore genesis.
692 Consequently, it is only through deciphering which indicator has been modified and by
693 what process (es) that S isotopes and S/Se ratios are able to provide a truly reliable

694 insight into the initial source of S. In addition, our trace element data allows us to assess
695 crustal contamination that may be linked with the S addition, but also other
696 contamination events, independently.

697 The dominance of $\delta^{34}\text{S}$ signatures in the GNPA member that are greater than the local
698 mantle range (Fig. 3A,B) suggests that, similar to many other magmatic sulfide PGE-Ni-
699 Cu deposits (e.g. Lesher and Groves 1986; Lesher and Burnham 2001; Li et al. 2002;
700 Ripley and Li 2003), the addition of crustal S through assimilation of S-bearing country
701 rocks was critical in the genesis of mineralization within the GNPA member. The
702 relatively high S/Se ratios within some of the primary sulfides support this. Typically,
703 contact-type PGE deposits are characterized by *in situ* contamination by local S-bearing
704 country rocks, which can either be responsible for ore formation (e.g. Duluth Complex;
705 Mainwaring and Naldrett 1977; Ripley 1981; Ripley et al. 1986 and the Basal Series of
706 the Stillwater Complex; Lambert et al. 1994; Lee 1996; McCallum 1996) or simply
707 overprint or modify an early developed crustal signature (e.g. Platreef; Holwell et al.
708 2007; McDonald and Holwell 2007; Penniston-Dorland et al. 2008; Ihlenfeld and Keays
709 2011). Whilst Maier et al. (2008) inferred a local control over the $\delta^{34}\text{S}$ composition of
710 sulfides within the GNPA member, the data in this study is inconsistent with the
711 contribution of S from the local footwall as: (i) a crustal component is evident in sulfides
712 developed east and west of the Grasvally Fault where underlain by quartzites and Lower
713 Zone cumulates; and (ii) there is no evidence that the degree of contamination increases
714 towards the footwall contact which is a feature commonly observed within the Platreef
715 where the magma has sufficiently interacted with the local footwall (e.g. Sharman-Harris
716 et al. 2005). In addition, the quartzites which underlie the GNPA member are themselves
717 an unlikely source of S as although sufficiently high $\delta^{34}\text{S}$ values are found in pyrite (+3.5
718 up to +10‰; Table 1; Fig. 3), S-bearing minerals are relatively scarce throughout the
719 Magaliesberg Quartzite Formation.

720 Although the use of S/Se ratios is complicated by the wider range of processes that can
721 alter the ratio from its initial value as discussed above, preservation of crustal S/Se ratios
722 within part of the primary sulfide assemblage in the GNPA provides evidence of an early
723 contribution of crustal S, consistent with the S isotope signatures. As these high S/Se
724 ratios (~6000) are preserved where the succession is underlain by Lower Zone cumulates,
725 they also indicate that the GNPA magma was emplaced saturated in sulfide with a

726 contaminated signature. Ihlenfeld and Keays (2011) used a similar argument for the
727 Platreef, where areas underlain by S-poor granites and gneisses consistently showed
728 crustal S/Se ratios.

729 As these findings are inconsistent with any model which involves the *in situ* development
730 of a sulfide liquid, but yet are characterised by some crustal S, it is concluded that the
731 magma from which the GNPA member crystallized was contaminated and saturated in S
732 prior to emplacement. Our trace element data also shows evidence that the entire package
733 was contaminated (Figs. 9,10). The consistency of the primitive mantle-normalized
734 spidergrams presented in Figure 9 demonstrate that the GNPA magma (s) was
735 characterised by pronounced negative Nb and Ti anomalies and LILE enrichment,
736 features also reflected in the low $(\text{Nb/Th})_{\text{PM}}$ ratios and high $(\text{Th/Yb})_{\text{PM}}$ ratios (Fig. 10).
737 Since these geochemical signatures are characteristic of crustal rocks and thus considered
738 indicative of crustal contamination of a mantle derived magma (Lightfoot and
739 Hawkesworth 1988; Lightfoot et al. 1990; Ihlenfeld and Keays 2011), it is inferred that
740 the parental magma(s) of the GNPA member were strongly crustally contaminated,
741 almost exactly as shown by Ihlenfeld and Keays (2011) for the Platreef, prior to
742 emplacement. Furthermore, this contaminant must have: (1) contained some crustal S,
743 which was the trigger for sulfide saturation in the parental GNPA magma, consistent with
744 the S isotope data; (2) been enriched in LILE; and (3) been characterised by elevated
745 primitive mantle normalised Th/Yb ratios (> 15). Sharman et al. (2013) demonstrated that
746 the crustal S present within the Platreef originated from shales or carbonates from the
747 Duitschland Formation of the Transvaal Supergroup and on the basis of S isotope
748 signatures, we suggest a similar source of crustal contaminant for the GNPA member.
749 This is in agreement with a multi-stage emplacement model similar to that proposed for
750 the Platreef (see Lee 1996; Kinnaird 2005; Holwell et al. 2007; McDonald and Holwell
751 2007; Ihlenfeld and Keays 2011; McDonald and Holwell 2011) and for the rest of the
752 Bushveld Complex (Penniston-Dorland et al. 2012).

753 An usual feature of the GNPA member is that the chromitites have very distinctive,
754 anomalously heavy $\delta^{34}\text{S}$ compositions around 2‰ heavier than the rest of the magmatic
755 succession. As this is such a lithology-specific feature it is possible that $\delta^{34}\text{S}$ was
756 fractionated during the formation of the chromitites, though such fractionations are not

757 documented and therefore speculative at best. Alternatively, they may represent a very
758 particular, more contaminated magma event that triggered the formation of chromitites.

759 In contrast to this major pre-emplacement contamination event, the effects of later
760 assimilation of crustal rocks are localised and preserved only where a metasedimentary
761 footwall exists beneath the GNPA. Evidence of this second contamination event is only
762 revealed by variations in the abundance of certain trace elements, and not in the S/Se
763 ratios and S isotopes (as they only indicate contamination by S). Where the GNPA
764 member is in contact with the Magaliesberg Quartzite Formation, a local footwall control
765 over the REE signatures of the succession is clearly observed (Fig. 8). Here, the LMF
766 especially, and the MANO unit to a lesser extent are characterised by: (i) elevated
767 absolute concentrations of REE; (ii) enrichment in LILEs; and (iii) fractionation of
768 LREE. As these features are more pronounced in the LMF unit that is in contact with the
769 quartzites, it is concluded that a second contamination event resulted from the interaction
770 of the GNPA magma with local footwall rocks at the time of emplacement, but that this
771 did not input any crustal S. The Platreef also records a second, localised contamination
772 event, but in many cases, this also includes the addition of S from a variety of other floor
773 rocks (Sharman-Harris et al. 2005; Holwell et al. 2007).

774 Our work indicates that the S isotope signatures of the sulfides in the GNPA member are
775 reliable indicators of the role of crustal S in ore genesis. However, it is important that in
776 deposits where secondary sulfide overprints are identified, that the S isotope signatures of
777 the most primary assemblages are sought for this purpose (Holwell et al. 2007). More
778 generally, S isotope data can distinguish the sources of S in multi-stage sulfide
779 parageneses; but only when coupled with robust mineralogy and petrology that clearly
780 characterises different stages. Furthermore, trace element data can be utilised in concert
781 to distinguish multiple stages of crustal contamination, with or without the addition of S.

782 *10.6. A model for the emplacement of the GNPA member*

783 In the northern limb of the Bushveld Complex, the Rustenburg Layered Suite has been
784 disturbed by several phases of faulting, all of which are thought to post-date emplacement
785 and consolidation of the intrusion (Truter, 1947; van Rooyen, 1954; de Villiers, 1967;
786 van der Merwe, 1978; Hulbert, 1983). Although the relationship between the Platreef and
787 GNPA member is masked by the NE trending Ysterberg-Planknek Fault, which marks the

788 final episode of faulting within the southern sector of the limb, they are, as discussed
789 above, considered by many to represent parts of the same succession (McDonald et al.
790 2005; Maier et al. 2008; van der Merwe 2008; Grobler et al. 2012).

791 On the basis of several key observations that are presented in this, and previous work
792 (Smith et al., 2011; 2014) it is envisaged that the GNPA member formed simultaneous to
793 and in an analogous manner to the Platreef in multiple stages, and from one or a number of
794 sub-chambers. Both deposits show similar constraints on the timing of emplacement,
795 the timing of sulfide saturation and enrichment in PGE relative to the intrusion of Lower
796 and Main Zone magmas, as indicated by field relations and the S isotope composition and
797 S/Se ratio of the initial sulfide liquid. Furthermore, both show two distinct stages of
798 contamination. From these relationships it can be inferred that both the Platreef and
799 GNPA parental magmas were emplaced saturated in sulfide onto consolidated Lower
800 Zone cumulates (van der Merwe 1978; Kinnaird et al. 2005) and were significantly
801 cooled prior to the intrusion of Main Zone magma, which throughout the northern limb
802 was emplaced as a S-understaturated, fertile magma with a separate PGE budget to the
803 underlying PGE-Ni-Cu sulfide deposits (Holwell and Jordaan 2006; Maier and Barnes
804 2010; McDonald and Harmer 2011; Lombard 2012; Holwell et al. 2013).

805 A schematic summary of the proposed multi-stage model for the emplacement of the
806 GNPA and Platreef, based on this, and a number of other studies cited here, is shown in
807 Figure 13 and can be summarised as follows:

- 808 • At depth in a staging chamber, magma passing through (possibly of Lower Zone
809 composition) assimilates S-bearing and LILE enriched country rocks (Stage 1,
810 Fig. 13A). Crustal S is likely derived from shales and carbonates of the
811 Duitschland Formation and possibly other units of the Transvaal Supergroup. The
812 contaminant is well homogenised with the magma, inducing sulfide saturation and
813 development of an immiscible sulfide liquid (Stage 2, Fig. 13A).
- 814 • Sulfide droplets become enriched in PGE, Ni, Cu and semi-metals through
815 interaction and processing of pre-GNPA magma (s) (Stage 3, Fig. 13A). It is
816 possible that, like the Platreef, the GNPA member sourced its PGE content from
817 the magma which was intruded to form the generally metal-depleted Lower zone
818 intrusions, which cooled and solidified (McDonald and Holwell 2007; McDonald

819 et al. 2009; McDonald and Holwell 2011; Stage 4, Fig. 13A).

820 • An early pulse of new magma invades previously established staging chambers,
821 (Stages 5-7, Fig. 13B). This sulfide-bearing magma represents the parental
822 magma to the GNPA member and possibly the Platreef. This magma then
823 entrained and transported the pre-formed PGE-rich sulfides, and intruded into the
824 Transvaal Supergroup to form the GNPA member and the Platreef (Stages 8-9,
825 Fig. 13B).

826 • Multiple influxes of sulfide-bearing hybrid magma intruded into the Transvaal
827 Supergroup to form the GNPA member. The addition of compositionally similar
828 magma is represented by the appearance of cumulus chromite and plagioclase,
829 which is attributed to the *in situ* mixing of new and residual fractionated magmas
830 (Stage 9, Fig. 13B).

831 • During emplacement, these magmas interacted with the local footwall rocks, with
832 the GNPA assimilating some quartzite. In contrast to the Platreef at Turfspruit and
833 Sandsloot, this second contamination event did not introduce additional crustal S
834 into the system (Stage 10, Fig. 13B), with primary sulfides in the GNPA member
835 retaining their initial crustal $\delta^{34}\text{S}$ signature. This event therefore had no control
836 over ore genesis within the GNPA member, but did affect the sulfide content and
837 PGM mineralogy of the Platreef (e.g. Hutchinson and Kinnaird, 2005; Holwell et
838 al., 2007; Stage 10, Fig 13B).

839 • Subsequent to emplacement, hydrothermal fluids, possibly derived from xenoliths
840 of calc-silicates and other floor rocks, altered much of the primary sulfide and
841 PGE mineralogy to a pyrite-millerite dominant assemblage (Smith et al. 2011).
842 This low temperature alteration (<250°C) resulted in: (i) S-loss, lowering the S/Se
843 ratio to below the mantle range; (ii) $\delta^{34}\text{S}$ to fractionate by +1.5 ‰ during pyrite
844 formation; (iii) the decoupling and remobilization of Pd, Au and to a lesser extent
845 Cu from sulfides on a centimetre to decimetre scale (Smith et al., 2014); and (iv)
846 the alteration of sulfide margins by tremolite, actinolite, chlorite and talc (Smith et
847 al., 2011).

848 • Following the emplacement of the GNPA member and the Platreef a significant

849 period of crystallization and cooling occurred (Holwell et al., 2005; Holwell and
850 Jordaan, 2006).

851 • The rest of the Main Zone magma was then intruded as a PGE-fertile magma
852 (Stages 11-13, Fig. 13C). This magma exploited the contact between the Lower
853 Mafic and Mottled Anorthosite units to produce a sill of Main zone, represented
854 by the Lower Gabbronorite unit (Stage 14, Fig. 12C) within the GNPA member.

855 • Sulfide saturation in the Main Zone magma formed the Ni-Cu-PGE
856 mineralization (Stage 15, Fig. 13C) observed at Moorddrift (Maier and Barnes
857 2010; Holwell et al., 2013), and other Main Zone hosted mineralization at the
858 Aurora project (Maier et al., 2008) and the Waterberg area (Lombard, 2012).

859 11. Conclusions

860 Although the primary application of S isotopes and S/Se ratios is as independent tracers
861 of the initial source of S in magmatic deposits, our case study illustrates that a number of
862 syn- and post-magmatic processes may affect one, or both of these such that they may
863 provide ambiguous data with respect to S source. Rather than these processes being
864 problematic, variations in the $\delta^{34}\text{S}$ signature and in particular S/Se ratio can reveal a
865 wealth of additional detail on a number of processes involved in the genetic history of a
866 Ni-Cu-PGE deposit. However, a prerequisite for being able to do this is to utilise other
867 independent petrological and mineralogical techniques that provide constraints on both
868 the timing and effect of various ore-forming and modifying processes. Since the S/Se
869 ratio is most susceptible to modification, this indicator has the ability to preserve detail on
870 processes including: partial dissolution of sulfide, R-factor variations, hydrothermal
871 alteration and S-loss. Utilizing both bulk and *in situ* methods in concert to determine the
872 S/Se ratio allows for the assessment of multiple sulfide populations, the partitioning
873 behaviour of Se during sulfide liquid fractionation and also the effects of low temperature
874 fluid alteration. In comparison, S isotopes are relatively more robust and represent a more
875 reliable indicator of the role of crustal S contamination, though the addition of trace
876 element data can reveal multiple stages of contamination that do not necessarily include
877 crustal S.

878 **Acknowledgements**

879 The authors would like to thank Caledonia Mining Corporation and in particular Trevor
880 Pearton, for allowing access to the drillcore on the farms Rooipoort, Grasvally and
881 Moorddrift; and Platinum Group Metals for allowing the sampling of core from War
882 Springs. Review by Reid Keays is acknowledged for improving the clarity and structure
883 of the manuscript, and editorial handling and review by Franco Pirjano. Jennifer Smith's
884 Ph.D. research was funded by the Natural Environment Research Council
885 (NE/1528426/1). The S isotope work was carried out via a NERC Facilities grant
886 (IP/1280/1111) awarded to DAH at the Isotope Community Support Facility at SUERC.
887 This work was part funded by a NERC SoS Minerals catalyst grant NE/L002191/1
888 awarded to the University of Leicester, and by a NERC SoS Consortium grant
889 NE/M010848/1 "TeaSe: tellurium and selenium cycling and supply" awarded to the
890 University of Leicester and Cardiff University. SUERC is supported by NERC and the
891 Scottish Universities consortium.

892

893 **References**

- 894 Arcuri T, Ripley EM, Hauck SA (1998) Sulfur and oxygen isotope studies of the
895 interaction between pelitic xenoliths and basaltic magma at the Babbitt and Serpentine
896 Cu-Ni deposits, Duluth Complex, Minnesota. *Economic Geology* 93:1063–1075.
- 897 Barnes S-J, Lightfoot PC (2005) Formation of magmatic nickel-sulfide ore deposits and
898 processes affecting their copper and platinum-group element contents. In: Hedenquist
899 JW, Thompson, JFH, Goldfarb RJ, Richards JP (eds.) *Economic Geology 100th*
900 Anniversary Volume 179–213.
- 901 Barnes S-J, Savard D, Bédard P, Maier WD (2009) Selenium and sulfur concentrations in
902 the Bushveld Complex of South Africa and implications for formation of the platinum-
903 group element deposits. *Mineralium Deposita* 44:647–663.
- 904 Brenan JM (2015) Se-Te fractionation by sulfide–silicate melt partitioning: Implications
905 for the composition of mantle-derived magmas and their melting residues. *Earth*
906 *Planetary Sci Lett*, 422:45-57
- 907 Buchanan DL, Nolan J, Suddaby P, Rouse JE, Viljoen MJ, Davenport JWJ (1981) The
908 genesis of sulfide mineralization in a portion of the Potgietersrus limb of the Bushveld
909 Complex. *Economic Geology* 76:568–579.
- 910 Cameron EM (1982) Sulphate and sulphate reduction in early Precambrian oceans.
911 *Nature* 296:145–148.
- 912 Cawthorn RG, Meyer FM (1993) Petrochemistry of the Okiep copper district basic
913 intrusive bodies, northwestern Cape province, South Africa. *Economic Geology* 88:590–
914 605
- 915 Chambers LA, Trudinger PA (1979) Microbiological fractionation of stable sulfur
916 isotopes: A review and critique. *Journal of Geomicrobiology* 1:249–293
- 917 Dare SA, Barnes SJ, Prichard HM, Fisher PC (2014) Mineralogy and Geochemistry of
918 Cu-Rich Ores from the McCreedy East Ni-Cu-PGE Deposit (Sudbury, Canada):
919 Implications for the Behaviour of Platinum Group and Chalcophile Elements at the End
920 of Crystallization of a Sulfide Liquid. *Economic Geology* 109:343–366

- 921 de Klerk L (2005) Bushveld Stratigraphy on Rooipoort, Potgietersrus Limb [abs.].
922 Platreef Workshop, 2nd, Mokopane, South Africa, 28th – 30th October 2005, Abstracts.
- 923 de Villiers, 1967, The geology of the area south of Potgietersrus, with special reference to
924 the chromite deposits: Ph.D. thesis, University of the Witwatersrand, 124 p.
- 925 Eckstrand OR, Cogolu E (1986) Se/S evidence relating to genesis of sulphides in the
926 Crystal Lake gabbro, Thunder Bay, Ontario. Geological Association of Canada –
927 Abstract Programs 11, 66.
- 928 Eckstrand OR, Hulbert LJ (1987) Selenium and the source of sulfur in magmatic nickel
929 and platinum deposits (abs): Geological Association of Canada–Mineralogical
930 Association Canada Program with Abstracts, v.12, p.40.
- 931 Eckstrand OR, Grinenko LN, Krouse HR, Paktunc AD, Schwann PL, Scoates RF (1989)
932 Preliminary data on sulphur isotopes and Se/S ratios, and the source of sulphur in
933 magmatic sulphides from the Foz River Sill, Molson Dykes and Thompson nickel
934 deposits, northern Manitoba. Current Research, Part C. Geological Survey of Canada
935 Paper 235–242.
- 936 Ewers GR (1977) Experimental hot water-rock interactions and their significance to
937 natural hydrothermal systems in New Zealand. *Geochimica et Cosmochimica Acta*
938 41:143–150.
- 939 Grassineau NV, Appel PWU, Fowler CMR, Nisbet EG (2005) Distinguishing biological
940 from hydrothermal signatures via sulphur and carbon isotopes in Archaean
941 mineralisations at 3.8 and 2.7 Ga. In: McDonald I, Boyce AJ, Butler IB, Herrington RJ,
942 Polya DA (eds) *Mineral deposits and earth evolution*. Geol Soc London 248:195–212
943 (special publication)
- 944 Grinenko LI (1985) Sources of sulfur of the nickeliferous and barren gabbro-dolerite
945 intrusions of the northwest Siberian platform. *International Geology Review* 27:695–708.
- 946 Grobler DF, Nielsen SA, Broughton DW (2012) Upper Critical Zone (Merenksy Reef)
947 correlates within the Platreef on Turfspruit 241KR, northern limb, Bushveld Complex:
948 Platreef Workshop, 5th, Mokopane, South Africa, 9th – 11th November 2012, Abstracts.

- 949 Habicht K, Canfield DE (1997) Sulfur isotope fractionation during bacterial sulfate
950 reduction in organic-rich sediments. *Geochimica et Cosmochimica Acta* 61:5351–5361
- 951 Hattori KH, Arai S, Clarke DB (2002) Selenium, tellurium, arsenic and antimony
952 contents of primary mantle sulfides. *Canadian Mineralogist* 40: 637–650.
- 953 Helmy HM, Ballhaus C, Wohlgemuth-Ueberwasser C, Fonseca RO, Laurenz V (2010)
954 Partitioning of Se, As, Sb, Te and Bi between monosulfide solid solution and sulfide
955 melt–Application to magmatic sulfide deposits. *Geochimica et Cosmochimica Acta*
956 74:6174–6179.
- 957 Hinchey JG, Hattori KH (2005) Magmatic mineralization and hydrothermal enrichment
958 of the High Grade Zone at the Lac des Iles palladium mine, northern Ontario, Canada.
959 *Mineral Deposita* 40: 13–23.
- 960 Holwell DA, Jordaan A (2006) Three-dimensional mapping of the Platreef at the
961 Zwartfontein South mine: implications for the timing of magmatic events in the northern
962 limb of the Bushveld Complex, South Africa. *Applied Earth Science (Transactions of the*
963 *Institute of Mining and Metallurgy B)* 115:B41–B48.
- 964 Holwell DA, Armitage PEB, McDonald I (2005) Observations on the relationship
965 between the Platreef and its hangingwall. *Applied Earth Science (Transactions of the*
966 *Institute of Mining and Metallurgy B)*, v. 114, p. B225–B241.
- 967 Holwell DA, McDonald I, Butler IB (2011) Precious metal enrichment in the Platreef,
968 Bushveld Complex, South Africa: evidence from homogenized magmatic sulfide melt
969 inclusions. *Contrib Mineral Petrol* 161:1011–1026
- 970 Holwell DA, Abraham-James T, Keays RR, Boyce AJ (2012) The nature and genesis of
971 marginal Cu–PGE–Au sulphide mineralisation in Paleogene Macrodykes of the
972 Kangerlussuaq region, East Greenland. *Mineral Deposita*, 47:3–21.
- 973
- 974 Holwell DA, Boyce AJ, McDonald I (2007) Sulfur isotope variations within the Platreef
975 Ni–Cu–PGE deposit: Genetic Implications for the origin of sulfide mineralization.
976 *Economic Geology* 102: 1091–1110.
- 977 Holwell DA, Jones A, Smith JW, Boyce AJ (2013) New mineralogical and isotopic

978 constraints on Main Zone-hosted PGE mineralisation at Moorddrift, northern Bushveld
979 Complex. *Mineral Deposita* 48:675–686.

980 Holwell DA, Keays RR, Firth EA, Findlay J (2014) Geochemistry and mineralogy of
981 platinum-group element mineralization in the River Valley intrusion, Ontario, Canada: a
982 model for early stage S saturation and multi-stage emplacement and the implications for
983 ‘contact-type’ Ni-Cu-PGE mineralization. *Economic Geology*.

984 Holwell DA, Keays RR, McDonald I, Williams MR (in revision) Extreme enrichment of
985 PGE, Au, Se and Te by sulfide droplets in closed system magma chambers: evidence
986 from LA-ICP-MS analysis of sulfide microdroplets in the Skaergaard Intrusion, east
987 Greenland. *Contr Mineral Petrol*

988 Howard JH (1977) Geochemistry of selenium: formation of ferroselite and selenium
989 behavior in the vicinity of oxidizing sulfide and uranium deposits. *Geochimica et*
990 *Cosmochimica Acta* 41: 1665–1678.

991 Hulbert LJ (1983) A petrographical investigation of the Rustenburg Layered Suite and
992 associated mineralization south of Potgietersrus. Unpublished D.Sc. dissertation, Pretoria,
993 South Africa, The University of Pretoria.

994 Hutchinson D, Kinnaird JA (2005) Complex multistage genesis for the Ni-Cu-PGE
995 mineralization in the southern region of the Platreef, Bushveld Complex, South Africa.
996 *Applied Earth Science* (Transactions of the Institute of Mining and Metallurgy B), v. 114,
997 p. B208–B223.

998 Ihlenfeld C, Keays R (2011) Crustal contamination and PGE mineralization in the
999 Platreef, Bushveld Complex, South Africa: evidence for multiple contamination events
1000 and transport of magmatic sulfides. *Mineralium Deposita* 46: 813–832.

1001 Kelley SP, Fallick AE (1990) High precision spatially resolved analysis of $\delta^{34}\text{S}$ in
1002 sulfides using a laser extraction system. *Geochimica et Cosmochimica Acta* 54: 883–888.

1003 Kerr A, Leitch AM (2005) Self destructive sulfide segregation systems and the formation
1004 of high-grade magmatic ore deposits. *Economic Geology* 100: 311–332.

- 1005 Kinnaird JA (2005) Geochemical evidence for multiphase emplacement in the southern
1006 Platreef. *Applied Earth Science* (Transactions of the Institute of Mining and Metallurgy
1007 B) 114: B225–B241.
- 1008 Kinnaird JA, Kruger FJ, Nex PAM, Cawthorn RG (2002) Chromitite formation—a key to
1009 understanding processes of platinum enrichment: *Applied Earth Science* (Transactions of
1010 the Institute of Mining and Metallurgy B), v. 111, p. B23–B35.
- 1011 Lambert DD, Walker RJ, Morgan JW, Shirey SB, Carlson RW, Zientek ML, Lipin BR,
1012 Koski MS, Cooper RL (1994) Re—Os and Sm—Nd Isotope Geochemistry of the
1013 Stillwater Complex, Montana: Implications for the Petrogenesis of the J-M Reef. *Journal*
1014 *of Petrology* 35: 1717–1753.
- 1015 Lee CA (1996) A review of mineralization in the Bushveld Complex and some other
1016 layered mafic intrusions. In: Cawthorn RG (ed) *Layered intrusions*. Elsevier Science,
1017 pp103–146
- 1018 Leshner CM (1989) Komatiite-associated nickel sulfide deposits. In: Whitney JA, Naldrett
1019 AJ (eds) *Ore deposition associated with magmas. Reviews in Economic Geology, Society*
1020 *of Economic Geologists* pp.45–102.
- 1021 Leshner CM, Groves DG (1986) Controls on the formation of komatiite-associated nickel-
1022 copper sulphide deposits. In: Friedrich GH, et al. (eds) *Geology and Metallogeny of*
1023 *Copper Deposits. Proc. 25th Int. Geol. Congr., Moscow, Springer, Berlin* (1986), pp 43–
1024 62.
1025
- 1026 Leshner CM, Burnham OM (2001) Multicomponent elemental and isotopic mixing in Ni-
1027 Cu-(PGE) ores at Kambalda, Western Australia. *Canadian Mineralogist* 39:421–446.
- 1028 Leshner CM, Keays RR (2002) Komatiite-associated Ni-Cu-(PGE) deposits: Geology,
1029 mineralogy, geochemistry and genesis. *Canadian Institute of Mining, Metallurgy and*
1030 *Petroleum, Special Volume* 54: 579–618.
- 1031 Li C, Ripley EM, Maier WD, Gomwe TES (2002) Olivine and S isotopic compositions of
1032 the Uitkomst Ni-Cu sulfide ore-bearing complex, South Africa: Evidence for S
1033 contamination and multiple magma emplacements. *Chemical Geology* 188: 149–159.

- 1034 Lightfoot PC, Hawkesworth CJ (1988) Origin of Deccan Trap lavas: evidence from
1035 combined trace element and Sr-, Nd-and Pb-isotope studies: *Earth and Planetary Science*
1036 *Letters*, 91:89–104.
- 1037 Lightfoot PC, Keays RR (2005) Siderophile and chalcophile metal variations in flood
1038 basalts from the Siberian trap, Noril'sk region: Implications for the origin of the Ni-Cu-
1039 PGE sulfide ores. *Economic Geology*, 100: 439–462.
- 1040 Lightfoot PC, Hawkesworth CJ, Devey CW, Rogers NW, Van Calsteren PWC (1990)
1041 Source and differentiation of Deccan Trap Lavas: implications of geochemical and
1042 mineral chemical variations. *Journal of Petrology* 31:1165–1200.
- 1043 Lombard K (2012) Exploration results and mineral resource estimate for the Waterberg
1044 Platinum Project: Coffey Mining, South Africa, 89 p.
- 1045 Lorand JP, Alard O, Luguet A, Keays RR (2003) Sulfur and selenium systematics of the
1046 subcontinental lithospheric mantle: inferences from the Massif Central xenolith suite
1047 (France). *Geochimica et Cosmochimica Acta* 67: 4137–4151.
- 1048 Maier WD, Barnes S-J (1996) Unusually high concentrations of magnetite at Caraiba and
1049 other Cu-sulfide deposits in the Curaca Valley, Bahia, Brazil. *Canadian Mineralogist*
1050 34:717–731.
- 1051 Maier WD, Barnes S-J (1998) Concentrations of rare earth elements in silicate rocks of
1052 the Lower, Critical and Main Zones of the Bushveld Complex. *Chem Geol* 150:85–103.
- 1053 Maier WD, Barnes S-J (2010) The petrogenesis of platinum-group element reefs in the
1054 Upper Main Zone of the Northern Lobe of the Bushveld Complex on the farm
1055 Moorddrift, South Africa/ *Econ Geol* 105:841–854.
- 1056 Maier WD, de Klerk WJ, Teigler B, Mitchell AA (1996) Cu/Pd and Cu/Pt of silicate
1057 rocks in the Bushveld Complex: implications for platinum-group element exploration:
1058 *Economic Geology* 91:1151-1158.
- 1059 Maier WD, de Klerk L, Blaine J, Manyeruke T, Barnes S-J, Stevens MVA, Mavrogenes
1060 JA (2008) Petrogenesis of contact-style PGE mineralization in the northern lobe in the

1061 Bushveld Complex: comparison of data from the farms Rooipoort, Townlands, Drenthe
 1062 and Nonnenweth. *Mineralium Deposita* 43: 255–280.

1063 Mainwaring PR, Naldrett AJ (1977) Country-rock assimilation and the genesis of Cu-Ni
 1064 sulfides in the Waterhen intrusion, Duluth Complex, Minnesota. *Economic Geology* 72:
 1065 1269–1284.

1066 Manyeruke TD, Maier WD, Barnes S-J (2005) Major and Trace Element Geochemistry
 1067 of the Platreef on the farm Townlands, northern Bushveld Complex. *South African*
 1068 *Journal of Geology* 108: 381–396.

1069 McCallum IS (1996) The Stillwater Complex. In: Cawthorn RG, (ed) *Layered Intrusions*.
 1070 Elsevier Science, pp 441–484.

1071 McDonald I, Harmer RE (2011) Cu–Ni–PGE mineralisation at Aurora is not Platreef, so
 1072 where does it fit in?: Platreef Workshop, 4th, Mokopane, South Africa, 14th-16th January
 1073 2011, Abstracts.

1074 McDonald I, Holwell DA (2007) Did lower zone magma conduits store PGE-rich
 1075 sulphides that were later supplied to the Platreef? *South African Journal of Geology* 110:
 1076 611–616.

1077 McDonald I, Holwell DA (2011) Geology of the northern Bushveld Complex and the
 1078 setting and genesis of the Platreef Ni-Cu-PGE Deposit. *Reviews in Economic Geology*
 1079 17: 297–327.

1080 McDonald I, Holwell DA, Armitage PEB (2005) Geochemistry and mineralogy of the
 1081 Platreef and ‘Critical Zone’ of the northern lobe of the Bushveld Complex, South Africa:
 1082 implications for Bushveld stratigraphy and the development of PGE mineralization.
 1083 *Mineralium Deposita* 40: 526–549.

1084 McDonald I, Holwell DA, Wesley B (2009) Assessing the potential involvement of an
 1085 early magma staging chamber in the generation of the Platreef Ni–Cu–PGE deposit in the
 1086 northern limb of the Bushveld Complex: a pilot study of the Lower Zone Complex at
 1087 Zwartfontein. *Applied Earth Science* (Transactions of the Institute of Mining and
 1088 Metallurgy B), v. 118, p.B5–B20.

- 1089 McDonald I, Jones RE, Holwell DA, Butler IB (2012) Platinum-group element tenors and
1090 S/Se ratios of Platreef sulphide melt inclusions [abs.]. Platreef Workshop, 5th, Mokopane,
1091 South Africa, 9th-12th January 2012, Abstracts.
- 1092 McDonough WF, Sun SS (1995) The composition of the earth. *Chemical Geology*
1093 120:223–253.
- 1094 Miyoshi T, Sakai H, Chiba H (1984) Experimental study of sulfur isotope fractionation
1095 factors between sulfate and sulfide in high temperature melts. *Geochemistry Journal*
1096 18:75–84.
- 1097 Mountain BW, Wood SA (1988) Chemical controls on the solubility, transport, and
1098 deposition of platinum and palladium in hydrothermal solutions: a thermodynamic
1099 approach. *Economic Geology* 83:492–510
- 1100 Mungall JE, Brenan J (2014) Partitioning of platinum-group elements and Au between
1101 sulfide liquid and basalt and the origins of mantle-crust fractionation of the chalcophile
1102 elements. *Geochim. Cosmochim. Acta* 125:265-289
- 1103 Naldrett AJ (2011) Fundamentals of Magmatic Sulfide Deposits. *Reviews in Economic*
1104 *Geology* 17: 1–50.
- 1105 Naldrett AJ, Wilson A, Kinnaird JA, Chunnett G. (2009). PGE Tenor and Metal Ratios
1106 within and below the Merensky Reef, Bushveld Complex: Implications for its Genesis. *J*
1107 *Petrol* 50:625-659.
- 1108 Ohmoto H, Rye RO (1979) Isotopes of sulfur and carbon. In: Barnes HL (ed)
1109 *Geochemistry of hydrothermal ore deposits*, 2nd ed: London, John Wiley and Sons, pp.
1110 509–567.
- 1111 Patten C, Barnes S J, Mathez EA, Jenner FE (2013) Partition coefficients of chalcophile
1112 elements between sulfide and silicate melts and the early crystallization history of sulfide
1113 liquid: LA-ICP-MS analysis of MORB sulfide droplets. *Chemical Geology* 358:176–188
- 1114 Peach CL, Mathez EA, Keays RR (1990) Sulfide melt-silicate melt distribution
1115 coefficients for the noble metals and other chalcophile metals as deduced from MORB:
1116 Implications for partial melting. *Geochimica et Cosmochimica Acta* 54: 3379–3389

- 1117 Peck DC, Keays RR (1990) Insights into the behaviour of precious metals in primitive, S-
1118 undersaturated magmas; evidence from the Heazlewood River Complex, Tasmania.
1119 Canadian Mineralogist 28: 553–577.
- 1120 Penniston-Dorland SC, Wing BA, Nex PAM, Kinnaird JA, Farquhar J, Brown M,
1121 Sharman ER (2008) Multiple sulfur isotopes reveal a magmatic origin for the Platreef
1122 platinum group element deposit, Bushveld Complex, South Africa. *Geology* 36: 979–982.
- 1123 Penniston-Dorland SC, Mathez EA, Wing BA, Farquhar J, Kinnaird JA, 2012, Multiple
1124 sulfur isotope evidence for surface-derived sulfur in the Bushveld Complex. *Earth Planet*
1125 *Sci Letters* 337-338:236-242
- 1126 Prichard HM, Knight RD, Fisher PC, McDonald I, Mei-Fu Zhou, Wang CY (2013)
1127 Distribution of platinum-group elements in magmatic and altered ores in the Jinchuan
1128 intrusion, China: an example of selenium remobilization by post magmatic
1129 fluids. *Mineralium Deposita* 48:767–786.
- 1130 Queffurus M, Barnes S-J (2015) A review of sulfur to selenium ratios in magmatic
1131 nickel-copper and platinum-group element deposits. *Ore Geology Reviews*, v. 69, p. 301-
1132 324.
- 1133 Ripley EM (1981) Sulfur isotopic abundances of the Dunka Road Cu-Ni deposit, Duluth
1134 Complex, Minnesota. *Economic Geology* 76:619–620.
- 1135 Ripley EM (1990) Se/S ratios of the Virginia Formation and Cu-Ni mineralization in the
1136 Babbitt area, Duluth Complex, Minnesota. *Economic Geology* 85:1935–1940.
- 1137 Ripley EM, Lambert DD, Frick LR (1986) Re-Os, Sm-Nd, and Pd isotopic constraints on
1138 mantle and crustal contributions to magmatic sulfide mineralization in the Duluth
1139 Complex. *Geochimica et Cosmochimica Acta* 62:3349–3365
- 1140 Ripley EM, Li C (2003) Sulfur isotope exchange and metal enrichment in the formation
1141 of magmatic Cu-Ni-(PGE) deposits. *Economic Geology* 98: 635–641.
- 1142 Ripley EM, Li C, Shin D (2002) Paragenesis assimilation in the genesis of magmatic Ni–
1143 Cu–Co sulfide mineralization at Voisey’s Bay, Labrador: $\delta^{34}\text{S}$, $\delta^{13}\text{C}$ and Se/S evidence.
1144 *Economic Geology* 97:1307–1318.

1145 Ripley EM, Park YR, Li C, Naldrett AJ (1999) Sulfur and oxygen isotopic evidence of
 1146 country rock contamination in the Voisey's Bay Ni–Cu–Co deposit, Labrador, Canada.
 1147 *Lithos* 47:53–68.
 1148
 1149 Robinson BW, Kusakabe M (1975) Quantitative preparation of sulfur dioxide for $^{34}\text{S}/^{32}\text{S}$
 1150 analyses from sulfides by combustion with cuprous oxide: *Analytical Chemistry* 47:
 1151 1179–1181.
 1152
 1153 Sharman-Harris E, Kinnaid JA, Harris C, Horstmann UE, Wing B (2005) A new look at
 1154 sulfide mineralization of the northern limb, Bushveld Complex: A stable isotope study.
 1155 *Applied Earth Science (Transactions of the Institute of Mining and Metallurgy B)* 114:
 B252–B263.
 1156
 1157 Sharman ER, Penniston-Dorland SC, Kinnaid JA, Nex PAM, Brown M, Wing BA
 1158 (2013) Primary origin of marginal Ni–Cu–(PGE) mineralization in layered intrusions: $\Delta^{33}\text{S}$
 evidence from the Platreef, Bushveld, South Africa. *Economic Geology* 108: 365–377.
 1159
 1160 Smith JW, Holwell DA, McDonald I (2011) The mineralogy and petrology of platinum-
 1161 group element-bearing sulfide mineralization within the Grasvalley Norite–Pyroxenite–
 1162 Anorthosite (GNPA) member, south of Mokopane, northern Bushveld Complex, South
 1163 Africa. *Applied Earth Science (Transactions of the Institute of Mining and Metallurgy B)*
 120: B158–B174.
 1164
 1165 Smith JW, Holwell DA, McDonald I (2014) Precious and base-metal geochemistry and
 1166 mineralogy of the Grasvalley–Norite–Pyroxenite–Anorthosite (GNPA) member, northern
 1167 Bushveld Complex, South Africa: implications for a multistage emplacement.
Mineralium Deposita, 49:667–692
 1168
 1169 Thériault RM, Barnes S-J (1998) Compositional variations in Cu–Ni–PGE sulfides of the
 1170 Dunka Road deposit, Duluth Complex, Minnesota: the importance of combined
 assimilation and magmatic processes. *Canadian Mineralogist* 36:869–886.
 1171
 1172 Truter FC (1947) A remarkable transcurrent fault near Potgietersrust, Transvaal:
Geological Society of South Africa, 501–15
 1173
 1174 van der Merwe MJ (1978) The geology of the basic and ultramafic rocks of the

1174 Potgietersrus limb of the Bushveld Complex: Ph.D. thesis (unpublished), South Africa,
 1175 University of the Witwatersrand.

1176 van der Merwe MJ (2008) The geology and structure of the Rustenburg Layered Suite in
 1177 the Potgietersrus/Mokopane area of the Bushveld Complex, South Africa: *Mineralium*
 1178 *Deposita* 43:405–419.

1179 Van Rooyen (1954) Die geologie van .n gedeelte van gebied 7 (Potgietersrus). Geological
 1180 Survey of South Africa, Pretoria, 116 p.

1181 Wagner T, Boyce AJ, Fallick AE (2002) Laser combustion analysis of $\delta^{34}\text{S}$ of sulfosalt
 1182 minerals: Determination of the fractionation systematics and some crystal-chemical
 1183 considerations. *Geochimica et Cosmochimica Acta* 66: 2855–2863.

1184 Westerlund KJ, Gurney JJ, Carlson RW, Shirey SB, Hauri EH, Richardson SH (2004) A
 1185 metasomatic origin for late Archean eclogitic diamonds: Implications from internal
 1186 morphology of diamonds and Re-Os and S isotope characteristics of their sulfide
 1187 inclusions from the Late Jurassic Klipspringer kimberlites. *South African Journal of*
 1188 *Geology* 107:119–130.

1189 Wood SA (2002) The aqueous geochemistry of the platinum–group elements with
 1190 applications to ore deposits. In: Cabri LJ (ed) *The Geology, Geochemistry, Mineralogy*
 1191 *and Mineral Beneficiation of Platinum–Group Elements*. Canadian Institute of Mining,
 1192 Metallurgy and Petroleum, Special Volume 54 pp 211–249

1193 Yamamoto M (1976) Relationship between Se/S and sulfur isotope ratios of
 1194 hydrothermal sulfide minerals. *Mineralium Deposita* 11:197–209.

1195

1196 Figure Captions

1197 Fig. 1 Geological map of the northern limb of the Bushveld Complex showing locality of
1198 boreholes sampled and farms referred to in the text (adapted from van der Merwe 2008).
1199 Inset map of the entire Bushveld Complex modified from Eales and Cawthorn (1996)

1200 Fig. 2 Summary of the sulfide assemblages observed within the GNPA member showing
1201 the key mineralogical and textural changes observed during low temperature alteration of
1202 A: a purely magmatic pyrrhotite (pn)-pentlandite (pn)-chalcopyrite (cpy) sulfide
1203 assemblage; B and C show variations in the extent of replacement by pyrite (py) and
1204 millerite (mil).

1205 Fig. 3 Range in $\delta^{34}\text{S}$ values for all observed sulfide phases within the GNPA member
1206 and its footwall for A: primary sulfide assemblage; B: secondary sulfide assemblage; C:
1207 sulfides developed within chromitites; and D: sulfides present within the local footwall
1208 and late-stage fracture fills. LZ indicates samples analysed with a Lower Zone footwall.

1209 Fig. 4A Sulfur in wt% versus Se (ppm) for different sulfide assemblages hosted within
1210 the GNPA member. B. PGE tenor (Pt + Pd in 100% sulfide), versus bulk S/Se ratio for
1211 samples within the GNPA member. Mantle S/Se range is taken from Eckstrand and
1212 Hulbert (1987). Data is overlain by different R-factor values which are taken from
1213 Queffurus and Barnes (2015).

1214 Fig. 5 Relationship between Pt+Pd tenor and Se tenor.

1215 Fig. 6 Selected LA-ICP-MS TRA spectra for A and B: primary pyrrhotite and
1216 pentlandite; C and D: primary chalcopyrite and pyrrhotite; E: pyrite replacing pentlandite;
1217 F: pyrite and chalcopyrite relicts; G: secondary pyrite developed within the GNPA
1218 member zoned in Co and As; and H: pyrite from the Magaliesberg Quartzite Formation.

1219 Fig. 7 Range in S/Se ratio for individual sulfide phases calculated from LA-ICP-MS for
1220 A: primary sulfide assemblage; B: secondary sulfide assemblage; C: sulfides developed
1221 within chromitites.

1222 Fig. 8 Chondrite normalized rare earth element plots for A: the mottled anorthosite unit
1223 where underlain by quartzites, B: the Lower Mafic unit where underlain by quartzites, C:
1224 footwall quartzites from the Magaliesberg Quartzite Formation (note the different scale

1225 on the y axis), D: the mottled anorthosite unit where underlain by Lower Zone, E: the
1226 Lower Mafic unit where underlain by Lower Zone, and F: the Lower Gabbro unit.
1227 Shaded fields on A, B and E represent data from Maier et al. (2008).

1228 Fig. 9 Primitive mantle-normalized trace element patterns for samples for A: the Mottled
1229 Anorthosite unit (MANO), B: the Lower Gabbro unit (LGN), C: the Lower Mafic
1230 unit (LMF), and D: quartzites from the Magaliesberg Quartzite Formation.

1231 Fig. 10 A: Plot of $(\text{Nb/Th})_{\text{PM}}$ vs $(\text{Th/Yb})_{\text{PM}}$ for samples from the GNPA member.
1232 Average compositions of N-MORB, Hawaiian (Mauna Loa) tholeiites and Transvaal
1233 sediments are also shown for reference. B: comparison with $(\text{Nb/Th})_{\text{PM}}$ and $(\text{Th/Yb})_{\text{PM}}$
1234 ratios from the Platreef (Ihlenfeld and Keays 2011).

1235 Fig. 11 Relationship between average $\delta^{34}\text{S}$ signature and bulk S/Se ratios in samples from
1236 Tables 1 and 2.

1237 Fig. 12 Comparison of bulk S/Se ratios and the S/Se ratio of individual sulfide phases. All
1238 S/Se ratios are plotted against bulk Pt+Pd tenor for A: primary sulfide assemblages and
1239 B: secondary sulfide assemblages including footwall samples.

1240 Fig. 13 A: Genetic model looking east, for the intrusion of Lower Zone-type, with sulfide
1241 immiscibility occurs in an intermediate staging chamber(s). See text for full explanation
1242 of numbered stages. B: Genetic model looking east, for the intrusion of Critical or Main
1243 zone type magma that mixes with residual magma to form hybrid magmas. These then
1244 entrained pre-formed sulfides to be emplaced as the GNPA member and the Platreef. See
1245 text for full explanation of numbered stages. C: Intrusion of the bulk of the Main Zone
1246 magma occurs after solidification of the GNPA member and Platreef. See text for full
1247 explanation of numbered stages

1248

1249 Tables

1250 Table 1 Results of all conventional (c) and laser (l) S isotope analyses for GNPA member
 1251 sulfides together with LA-ICP-MS determined S/Se ratios. See Figure 1 for location of
 1252 boreholes. Lithological abbreviations: MA mottled anorthosite, PYX pyroxenite, CPX
 1253 clinopyroxenite, OPX orthopyroxenite, GBN gabbronorite, NR norite, CR chromitite,
 1254 QTZ quartzite. Sulfide abbreviations cpy chalcopyrite, cub cubanite, po pyrrhotite, pn
 1255 pentlandite, py pyrite, mil millerite, py* basement pyrite.

Borehole/depth	Lithology	Unit	Phase	Sulfide assemblage	$\delta^{34}\text{S}$ (‰ VCDT)	Technique	<i>in situ</i> S/Se
RP04.23 – Rooipoort, Lower Zone footwall							
157	MA	MANO	py	s	5.0	l	2318
191	PYX	MANO	pn	p	4.0	l	4148
191	PYX	MANO	pn	p	4.0	l	2147
191	PYX	MANO	cpy	p	2.8	l	
201	GBN	LGN	po	s	2.7	l	
305	NR	LMF	po	p	2.8	l	
330	GBN	LMF	po	p	2.0	c	
338	CPX	LMF	po	p	2.9	c	
384	GBN	LMF	po	p	3.5	c	
392	GBN	LMF	po	p	3.4	c	5297
392	GBN	LMF	po	p	3.5	c	4370
392	GBN	LMF	po	p	3.6	l	5335
392	GBN	LMF	cub	p	3.4	l	3289
392	GBN	LMF	cub	p			3156
392	GBN	LMF	cub	p			3466
392	GBN	LMF	pn	p	5.1	l	2613
392	GBN	LMF	pn	p	5.3	l	3621
396	GBN	LMF	po	p	3.3	c	
411	GBN	LMF	po	p	3.1	c	4800
411	GBN	LMF	po	p	3.2	l	2756
411	GBN	LMF	cub	p	4.0	l	4083
411	GBN	LMF	pn	p	5.0	l	4136
RP05.45 – Rooipoort, quartzite footwall							
146	GBN	LMF	py	s	6.8	l	3764
149	GBN	LMF	mil	s	3.9	l	
149	GBN	LMF	mil	s	3.6	l	
149	GBN	LMF	py	s	5.0	l	
149	GBN	LMF	py	s	4.2	l	
149	GBN	LMF	cpy	s	4.7	l	
165	GBN	LMF	cub	s	4.1	l	3535
165	GBN	LMF	cub	s	3.9	l	4776
165	GBN	LMF	py	s	3.9	l	4180
165	GBN	LMF	py	s	4.9	l	8267
165	GBN	LMF	py	s	4.9	l	4233
165	GBN	LMF	py	s		l	3948
165	GBN	LMF	mill	s	4.9	l	

166	CR	LMF	py	s	6.9	c	8611
166	CR	LMF	py	s	5.8	l	8546
166	CR	LMF	cub	s	5.3	l	5146
166	CR	LMF	cub	s			4116
166	CR	LMF	mil	s			2305
167*	CR	LMF	py	s	6.6	l	>8915 (min value as Se BDL)
167	CR	LMF	py	s	6.1	l	3364
167	CR	LMF	py	s	6.9	l	5183
167	CR	LMF	py	s	7.1	l	4863
167	CR	LMF	cub	s	5.4	l	1877
167	CR	LMF	cub	s	6.1	l	4096
167	CR	LMF	cub	s	4.4	l	4412
167	CR	LMF	cpy	s	4.4	l	
167	CR	LMF	cpy	s	2.8	l	
167	CR	LMF	pn	s	5.4	l	1919
167	CR	LMF	pn	s	5.6	l	2662
167	CR	LMF	pn	s	7.5	l	3015
167	CR	LMF	mill	s			2420
205	NR	LMF	py	s	4.1	l	
205	NR	LMF	py	s	4.3	l	
205	NR	LMF	mil	s	4.1	l	
205	NR	LMF	cpy	s	3.8	l	
206	CPX	LMF	cpy	s	3.9	l	
208	NR	LMF	py	s	5.0	l	8829
208	NR	LMF	py	s	4.9	l	3047
208	NR	LMF	py	s			5612
208	NR	LMF	pn	s	6.0	l	3695
208	NR	LMF	pn	s	5.8	l	2035
208	NR	LMF	pn	s			2325
208	NR	LMF	cub	s	5	l	2134
212	QTZ	FLR	py *	b	4.5	l	
212	QTZ	FLR	py *	b	4.1	l	
214	QTZ	FLR	py *	b	5.3	l	7731
214	QTZ	FLR	py *	b	5.6	l	8441
214	QTZ	FLR	py *	b	6.2	l	6916
214	QTZ	FLR	cub	s	3.6	l	3052
214	QTZ	FLR	cub	s	4.1	l	5917
214	QTZ	FLR	cub	s	4.5	l	
214	QTZ	FLR	mil	s	5.6	l	2217
214	QTZ	FLR	py	s	4.3	l	6476
215	QTZ	FLR	py *	b	4.1	c	6693
215	QTZ	FLR	py *	b	3.5	c	7875
215	QTZ	FLR	py *	b			5943

RP04.21 – Rooipoort, quartzite footwall

448	MA	MANO	cpy	s	3.5	l	
448	MA	MANO	py	s	4.1	l	
448	MA	MANO	py+mil	s	3.6	l	
460	MA	MANO	po	p	2.3	l	
460	MA	MANO	po	p	2.5	l	
679	MA	MANO	py	s	3.5	l	8980

679	MA	MANO	py	s	3.0	I	3619
679	MA	MANO	py	s			5693
679	MA	MANO	po	s	1.7	I	2797
679	MA	MANO	po	s			3494
679	MA	MANO	po	s			2802
679	MA	MANO	pn	s	3.2	I	2126
679	MA	MANO	pn	s			2517
679	MA	MANO	cub	s	1.3	I	3328
679	MA	MANO	cub	s			2709
681	MA	MANO	cpy	s	2.8	I	
681	MA	MANO	pn+mil	s	2.4	I	
690	GBN	MANO	po	p	1.6	I	3564
690	GBN	MANO	po	p	1.9	I	3391
690	GBN	MANO	po	p	1.8	I	2592
690	GBN	MANO	po	p	2.9	I	3562
690	GBN	MANO	pn	p			2941
690	GBN	MANO	cpy	p			4004
693	GBN	MANO	po	p	2.6	I	4409
693	GBN	MANO	po	p	3.1	I	3922
693	GBN	MANO	po	p			3456
693	GBN	MANO	pn	p	4.0	I	2032
693	GBN	MANO	pn	p	4.7	I	3680
693	GBN	MANO	cpy	p	3.3	I	4008
MD03.1 – Moorddrift, Lower Zone footwall							
552	OPX	MANO	pn	s	3.5	I	2106
552	OPX	MANO	cub	s	2.4	I	2961
552	OPX	MANO	cub	s	2.9	I	2272
542	QTZ vein	MANO	cpy	s	8.1	c	
542	QTZ vein	MANO	cpy	s	8.0	c	
573	fracture fill	MANO	cpy	s	11.4	c	
573	fracture fill	MANO	cpy	s	11.9	c	
RP05.37 – Rooipoort, quartzite footwall							
106	GBN	MANO	py	s	4.0	I	
RP03.12 – Rooipoort, quartzite footwall							
140	GBN	LMF	py	s	2.3	I	
140	GBN	LMF	py	s	3.6	I	
144	PYX	LMF	py	s	4.5	I	
145	Cr	LMF	py	s	4.8	I	
GV05.49 – Grasvally, quartzite footwall							
127	Cr	LMF	py	s	4.3	I	
127	Cr	LMF	cpy	s	3.6	I	
128	Cr	LMF	py	s	6.3	I	
128	Cr	LMF	cpy	s	5.7	I	
128	Cr	LMF	pn	s	5.1	I	
140	GBN	LMF	po	s	4.0	I	
140	GBN	LMF	po	s	4.7	I	
140	GBN	LMF	cpy	s	3.2	I	
140	GBN	LMF	py	s	3.6	I	
214	QTZ	FLR	py*	b	10.5	I	
214	QTZ	FLR	py*	b	9.8	I	
ORL 4 – War Springs, quartzite footwall							
65	MA	MANO	py	s	3.5	I	

65	MA	MANO	pn	s	3.8	I
65	MA	MANO	cpy	s	2.9	I
221	PYX	LMF	cpy	s	1.9	I
221	PYX	LMF	py	s	2.6	I
221	PYX	LMF	py	s	2.4	I
221	PYX	LMF	po	s	1.9	I
221	PYX	LMF	po	s	0.9	I
395	PYX	LMF	po	s	3.7	I
395	PYX	LMF	po	s	4.2	I
395	PYX	LMF	py	s	2.6	I
395	PYX	LMF	pn	s	4.2	I
606	CR	LMF	po	s	5.5	I
606	CR	LMF	po	s	5.3	I
606	CR	LMF	po	s	5.8	I
606	CR	LMF	po	s	5.3	I
606	CR	LMF	cpy	s	5.1	I
606	CR	LMF	cpy	s	5.9	I
606	CR	LMF	po	s	4.6	I
ORL5 – War Springs, quartzite footwall						
97	MA	MANO	py	s	3.2	I
97	MA	MANO	py	s	3.2	I
108	GBN	LMF	py	s	2.6	I
108	GBN	LMF	cpy	s	2.6	I
597	PYX	LMF	py	s	5.1	I
597	PYX	LMF	py	s	5.0	I
597	PYX	LMF	pn	s	5.8	I

S/Se ratios that are in italics represent the mean of several mineral analyses with comparable/Se ratios

1256

1257

1258 Table 2 Whole rock S and Se for primary (p) and secondary (s) sulfide-bearing samples
 1259 within the GNPA member together with PGE tenors (calculated using Barnes and
 1260 Lightfoot 2005 formula). Abbreviations FLR floor rocks (quartzites), LMF Lower Mafic
 1261 Unit, MANO Mottled Anorthosite Unit and Cr chromitite.

Borehole	Sample/ depth	Unit	Sulfide type primary/ secondary	Se (ppm)	S wt %	S/Se	Pt+Pd (ppb)	Pd in 100% sulfide (ppm)	Pt+Pd in 100% sulfide (ppm)
RP04.23	144	MANO	p	6.10	2.108	3456	1168	17	20
	157	MANO	s	3.00	0.806	2686	932	38	43
	201*	MANO	s	<0.20	0.084	4210*	143	41	61
	300	CR	p	1.50	0.266	1773	978	40	127
	305	LMF	p	3.50	0.751	2145	129	4	6
	338	LMF	p	0.70	0.292	4175	281	9	36
	384	LMF	p	0.70	0.406	5804	167	12	15
	392	LMF	p	0.90	0.512	5692	161	8	11
	411	LMF	p	0.70	0.434	6195	85	5	7
RP05.45	146	LMF	s	0.40	0.123	3067	139	34	49
	165	LMF	s	0.20	0.135	6765	126	27	36
	167	CR	s	2.10	0.735	3500	3603	85	153
	205	LMF	s	2.50	0.374	1494	1454	132	154
	208	LMF	s	0.50	0.080	1596	520	157	231
	215	FLR	s	1.20	0.428	3566	760	50	61
	214	FLR	s	8.30	3.340	4024	3389	26	36
RP04.21	448	MANO	s	1.00	0.379	3786	1064	70	103
	681	MANO	s	0.90	0.368	4083	474	33	48
	690	MANO	p	4.40	1.650	3750	1283	23	29
	693	MANO	p	2.00	0.808	4038	1048	31	48
MD03.1	552	MANO	s	4.70	0.991	2108	1915	32	66
GV02.1	166	MANO	p	3.90	1.468	3765	2115	46	56
	476	LMF	s	3.20	1.856	5800	675	7	13

201* S/Se ratio is a minimum value as detection limit is 0.2 for Se.

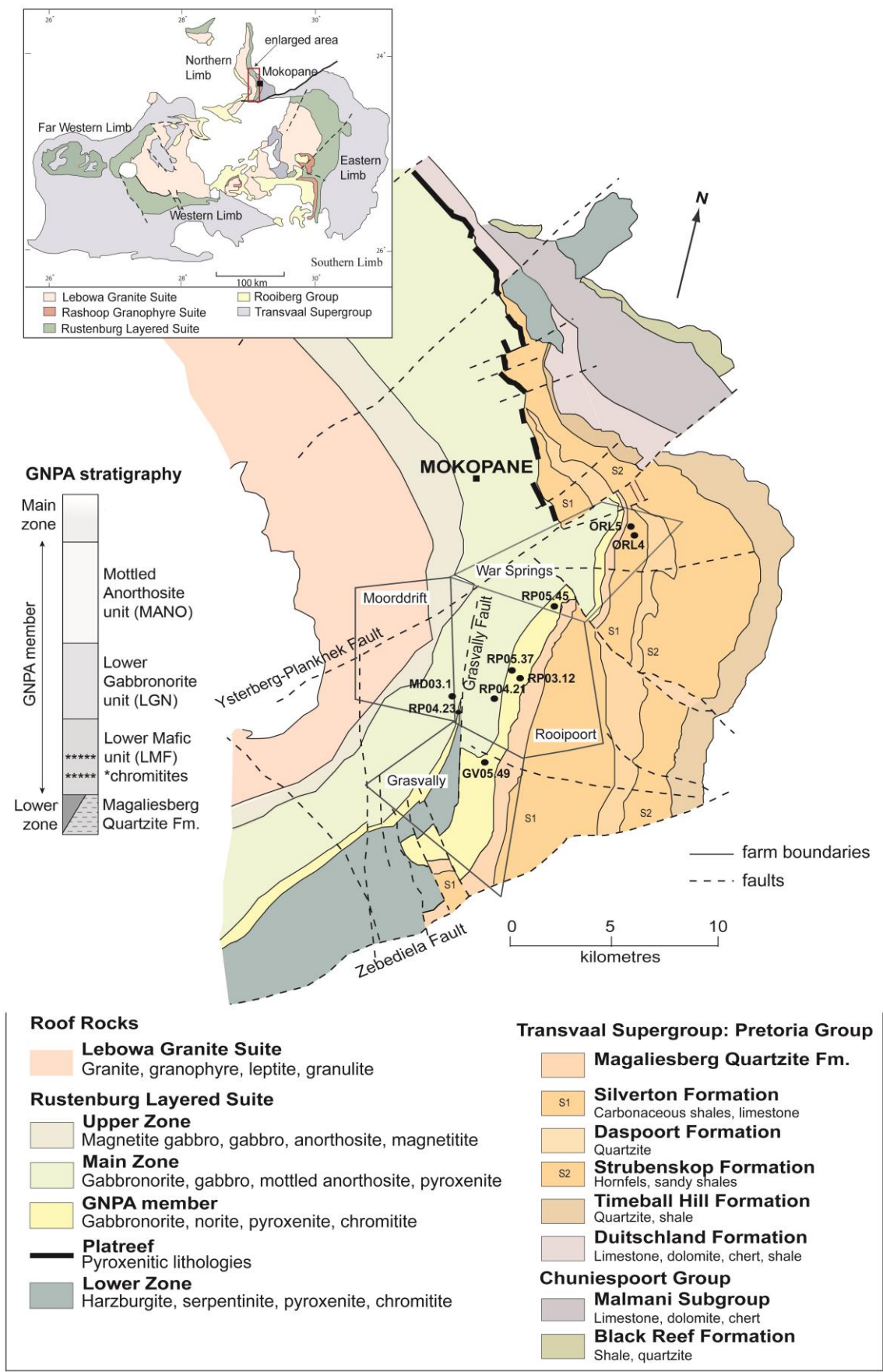
Table 3 Average LA-ICP-MS determined Se concentrations of pyrrhotite, pentlandite and chalcopyrite/cubanite in primary and secondary sulfide assemblages, together with low temperature pyrite and millerite. To reduce the error associated with the ratios all values <80 ppm have been excluded. Note the detection limit for Se is 60 ppm. An indication of the analytical error is propagated from using the average 12% counting variation observed on the in house Cardiff standard which contains 108 ppm Se.

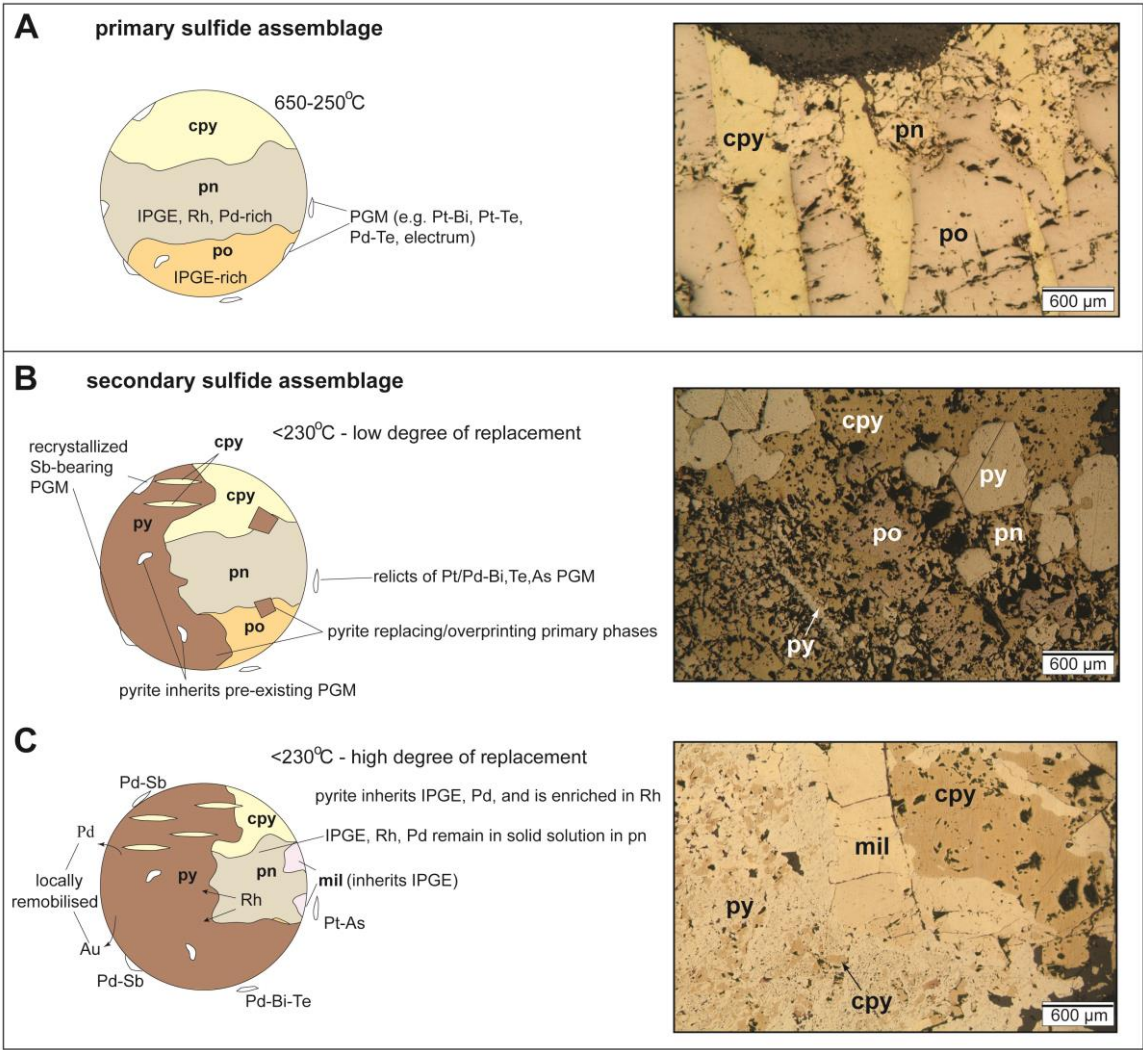
Se concentration in ppm											
Sample	po	pn	cpy/cub	py	mil	po:pn	po:cpy	pn:cpy	py:pn	py:cpy	py:mil
RP04.23/392											
MIN		92	102								
MAX	88	128	112								
MEAN	88	110	107			0.8±0.1	0.8±0.1	1.0±0.1			
ERROR	11	13	13								
n	1	2	3								
RP04.23/411											
MIN	80		85								
MAX	139	83	89								
MEAN	109	83	87			1.3±0.2	1.3±0.2	1.0±0.1			
ERROR	13	10	10								
n	2	2	2								
RP04.21/690											
MIN	97	103	86								
MAX	161	127	91								
MEAN	114	115	89			1.0±0.1	1.3±0.2	1.3±0.2			
ERROR	14	14	11								
n	11	3	2								
RP04.21/679											
MIN	108	109	107	110							
MAX	140	156	131	148							
MEAN	129	135	119	135		1.0±0.1	1.1±0.1	1.1±0.2	1.0±0.1	1.1±0.2	
ERROR	16	16	14	16							
n	5	5	2	3							
RP04.21/693											
MIN	85	90									
MAX	109	164									
MEAN	97	127				0.8±0.1					
ERROR	12	15									
n	3	2									
RP05.45/165											
MIN				128							
MAX			100	137							
MEAN			100	131						1.3±0.2	
ERROR			12	16							
n			1	3							
RP05.45/166-chromitite											
MIN					152						
MAX					593						
MEAN		214	85		345			2.5±0.2			
ERROR		26	10		41						
n		1	1		4						
RP05.45/167-chromitite											
MIN		103	84	103	134						
MAX		173	183	159	162						
MEAN		127	134	125	148			1.0±0.1	1.0±0.1	0.9±0.1	0.8±0.1
ERROR		15	16	15	18						
n		4	2	5	2						
RP05.45/208											
MIN		91		106							
MAX		164		229							
MEAN		140	121	165	131			1.2±0.2	1.2±0.2	1.4±0.2	1.3±0.2
ERROR		17	15	20	16						
n		8	1	8	1						
RP05.45/214											
MIN					153						
MAX					166						
MEAN			116		159						

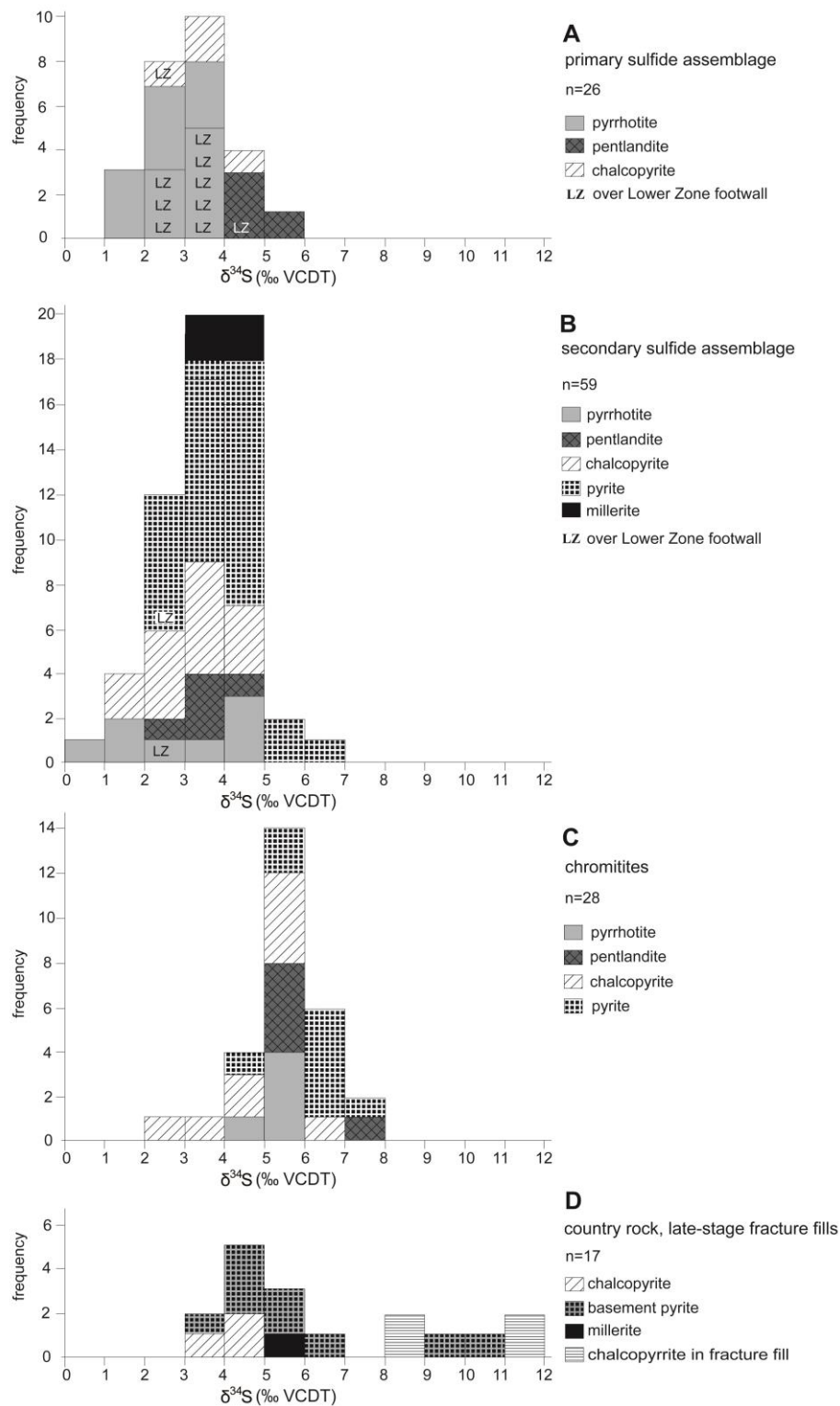
ERROR		14	19	
n		1	2	
MD03.1/552				
MIN	120	161		
MAX	156	155		
MEAN	138	158		0.9±0.1
ERROR	17	19		
n	2	2		

1269

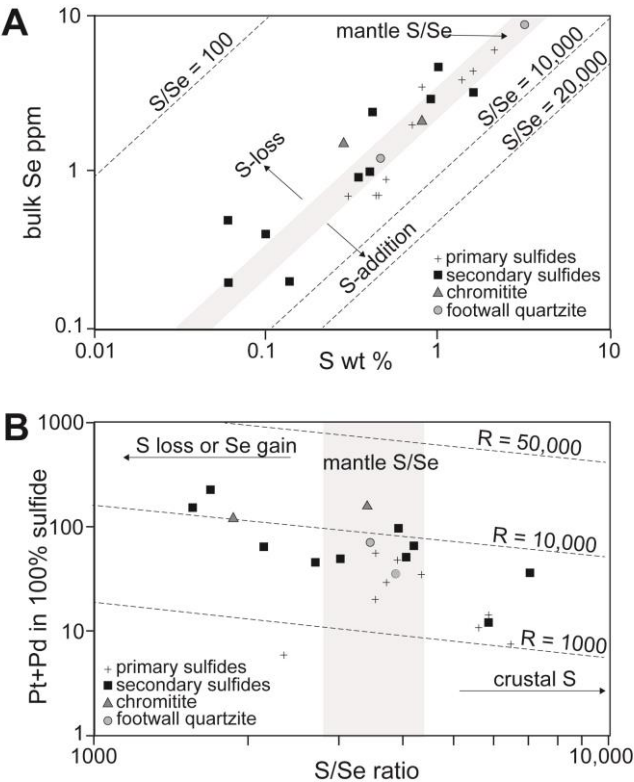
1270







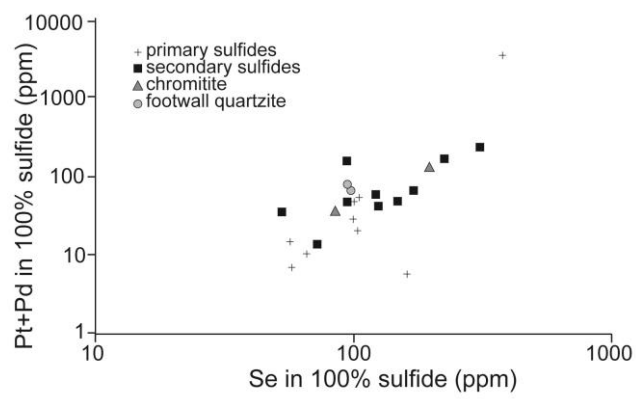
1279 Fig 4



1280

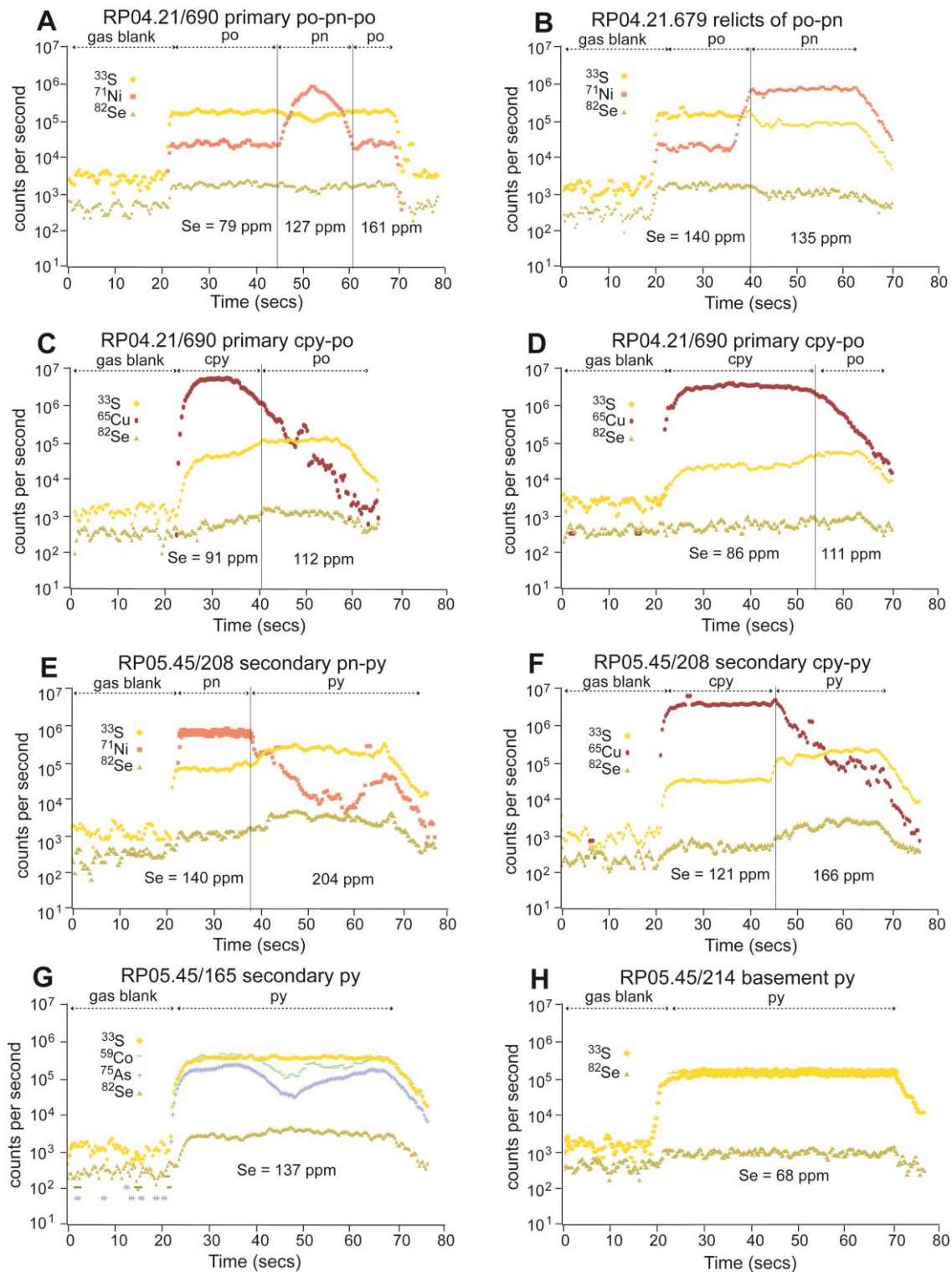
1281

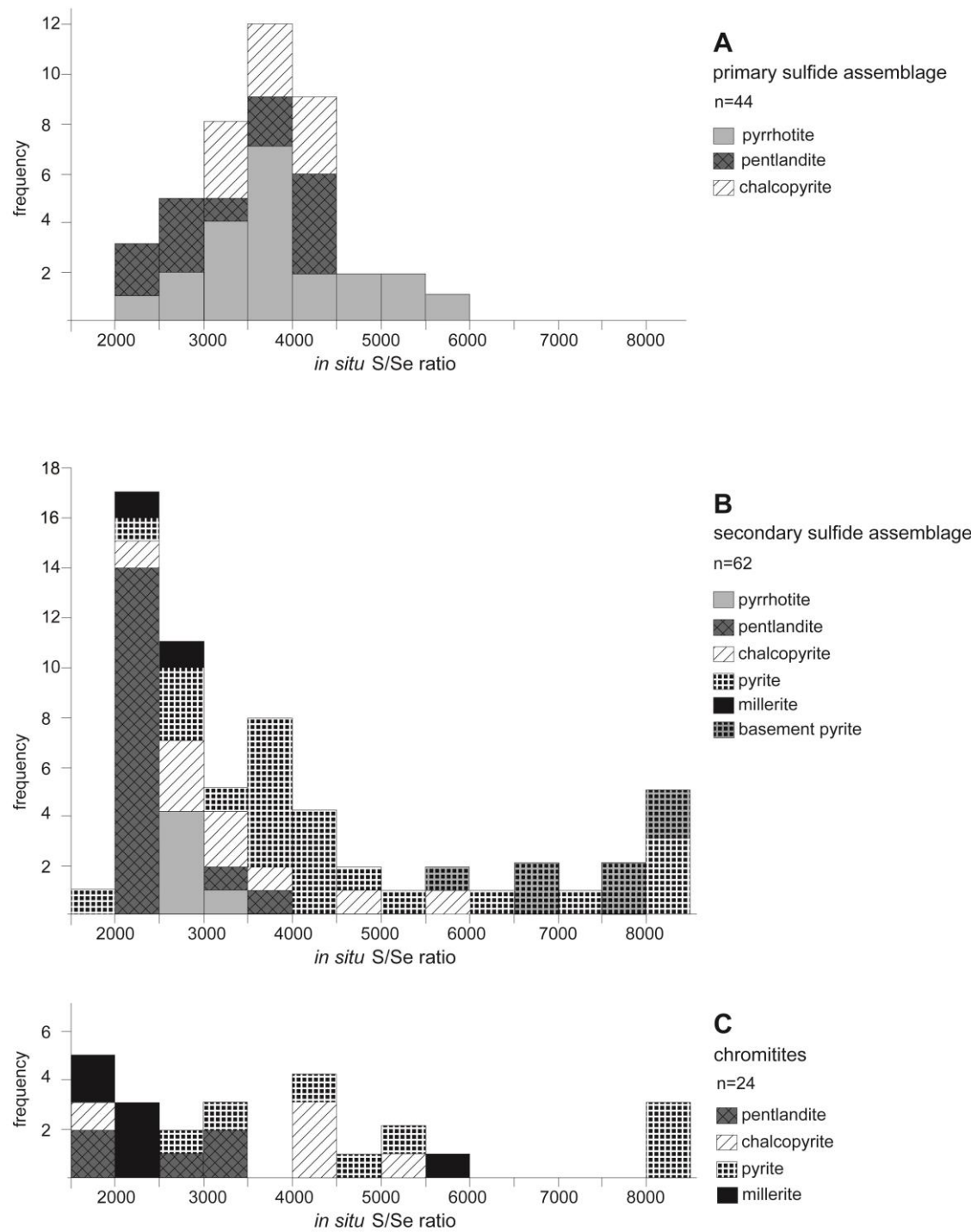
1282 Fig 5



1283

1284



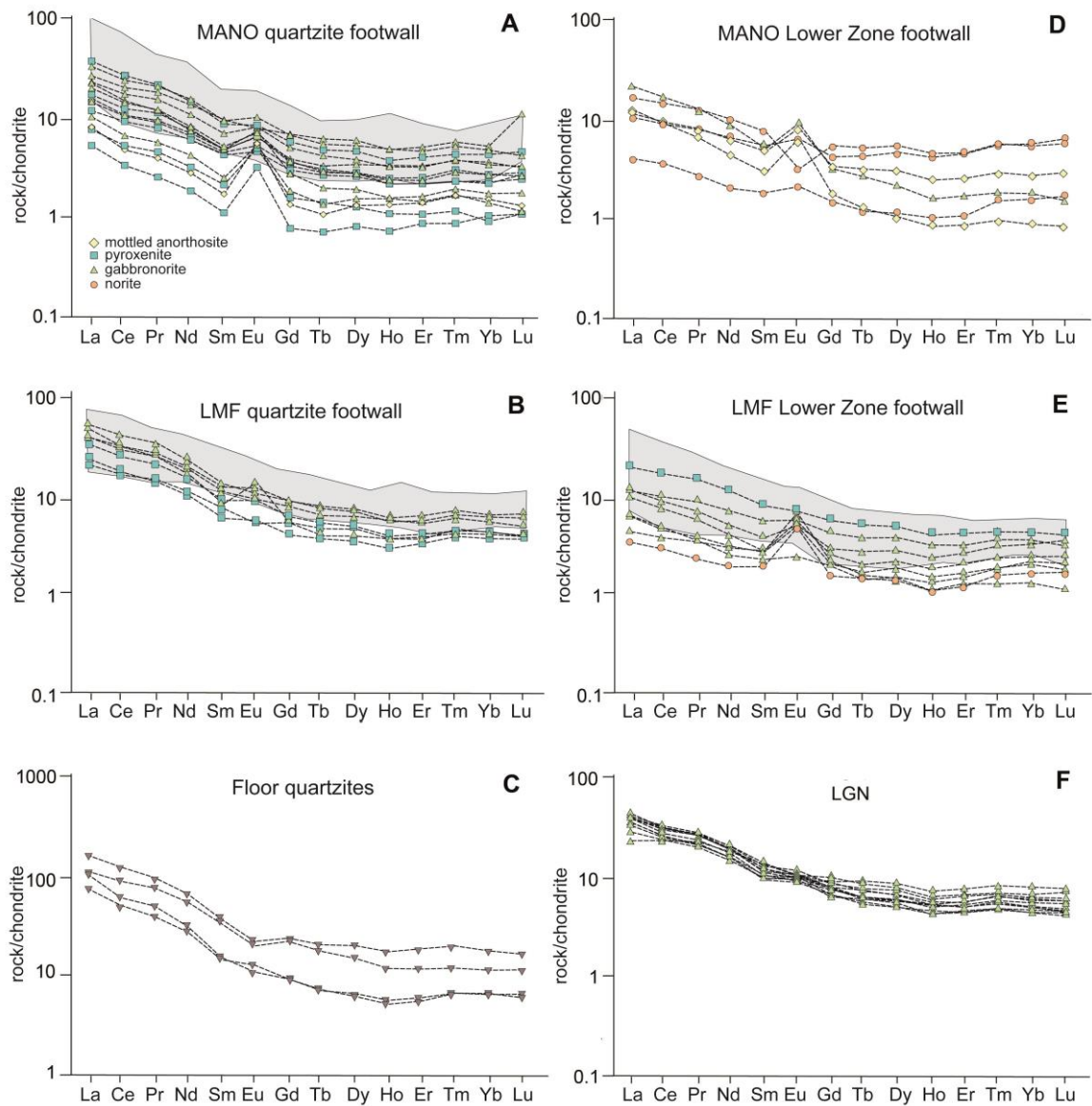


1289

1290

1291

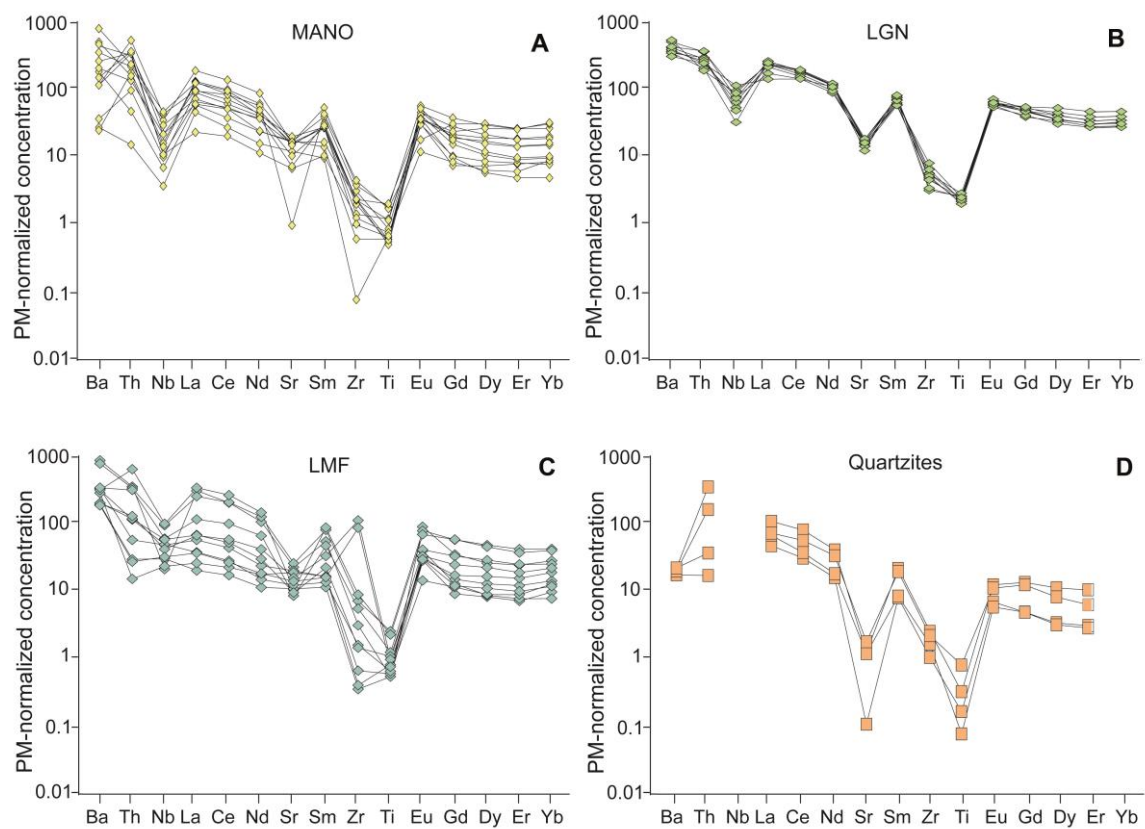
1292 Fig 8



1293

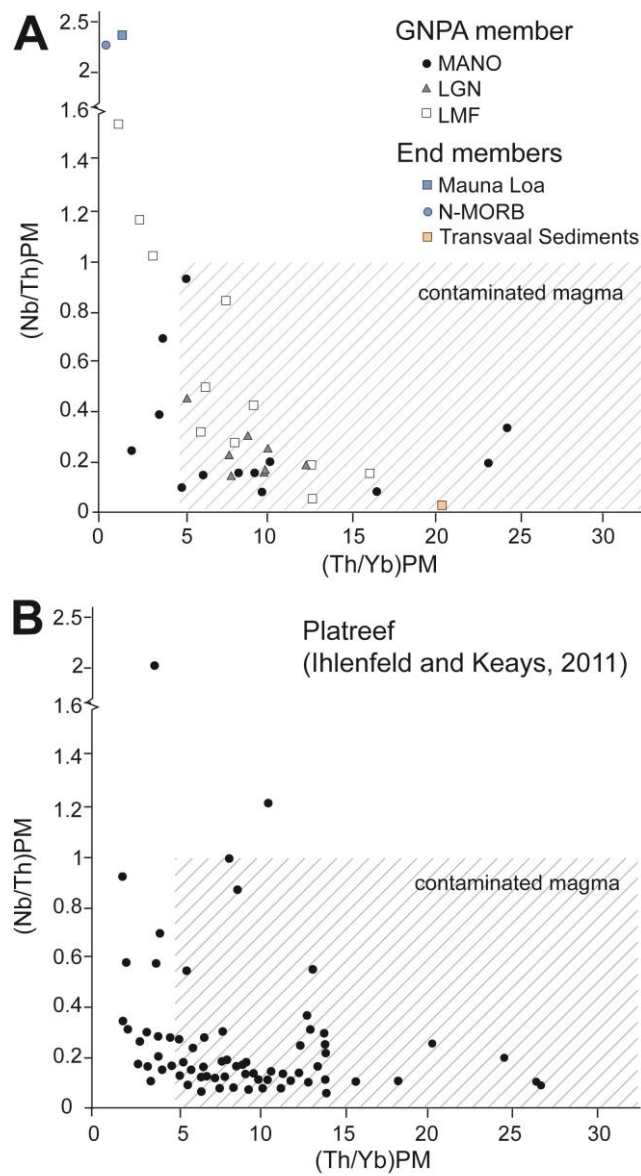
1294

1295 Fig 9

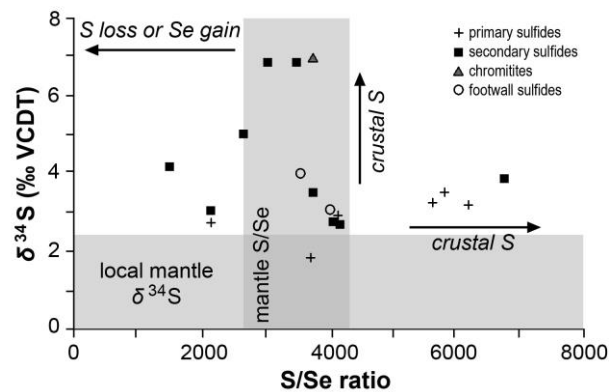


1296

1297

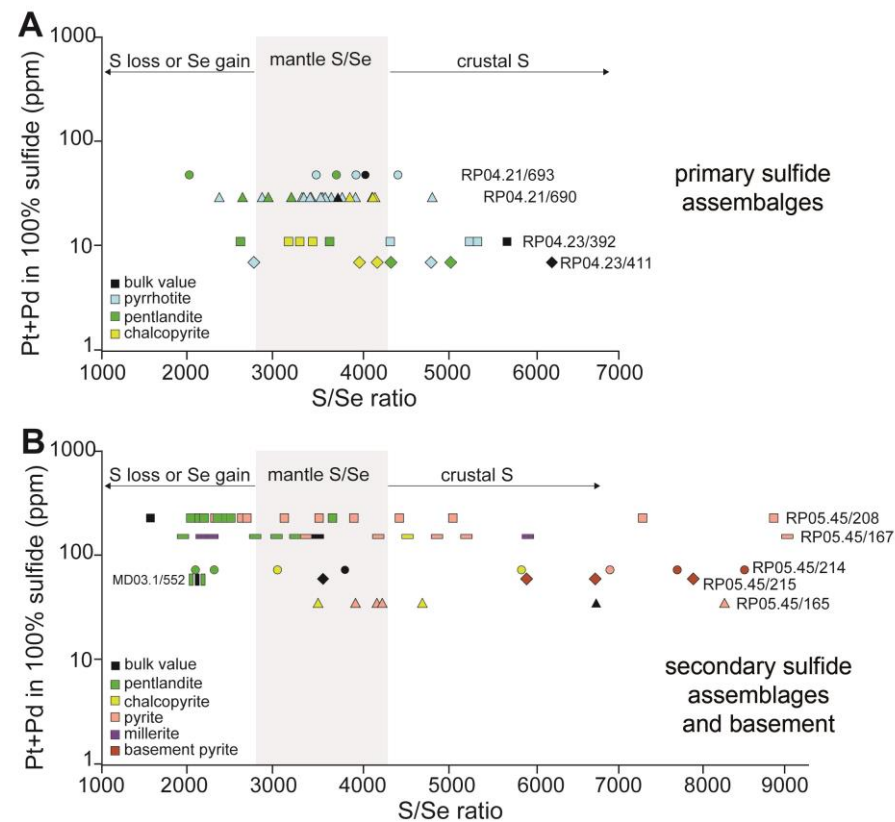


1301 Fig 11



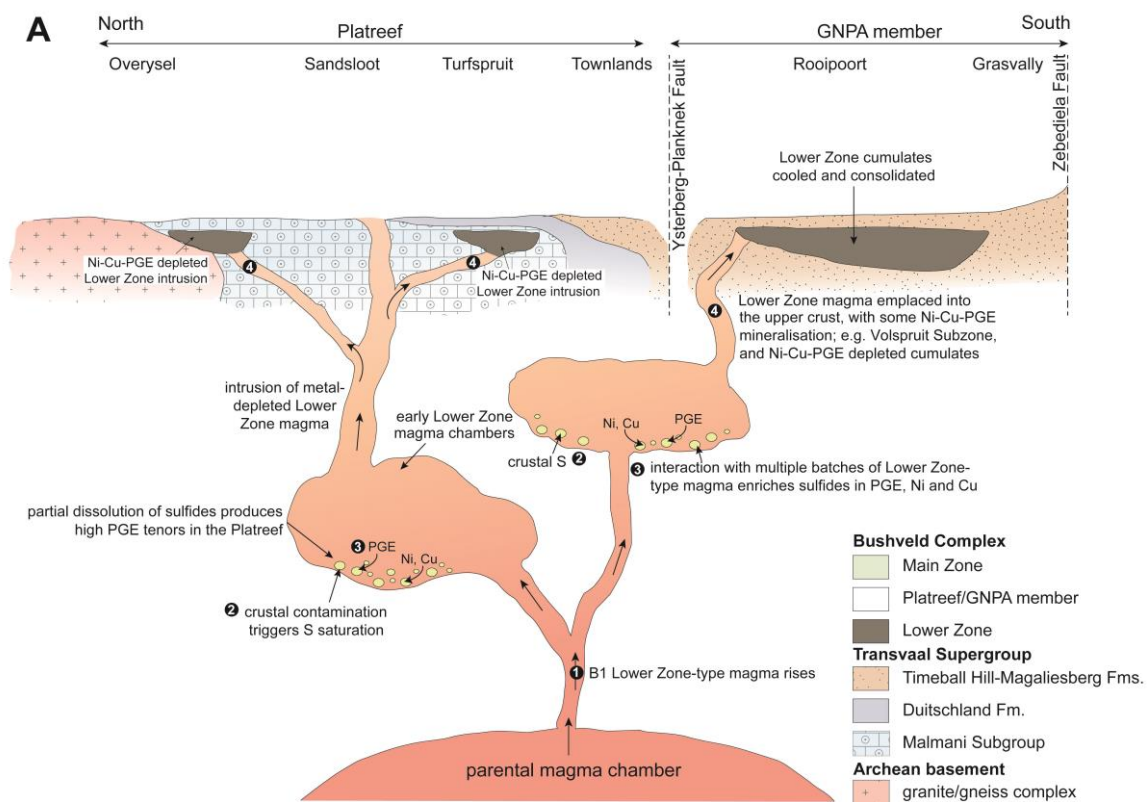
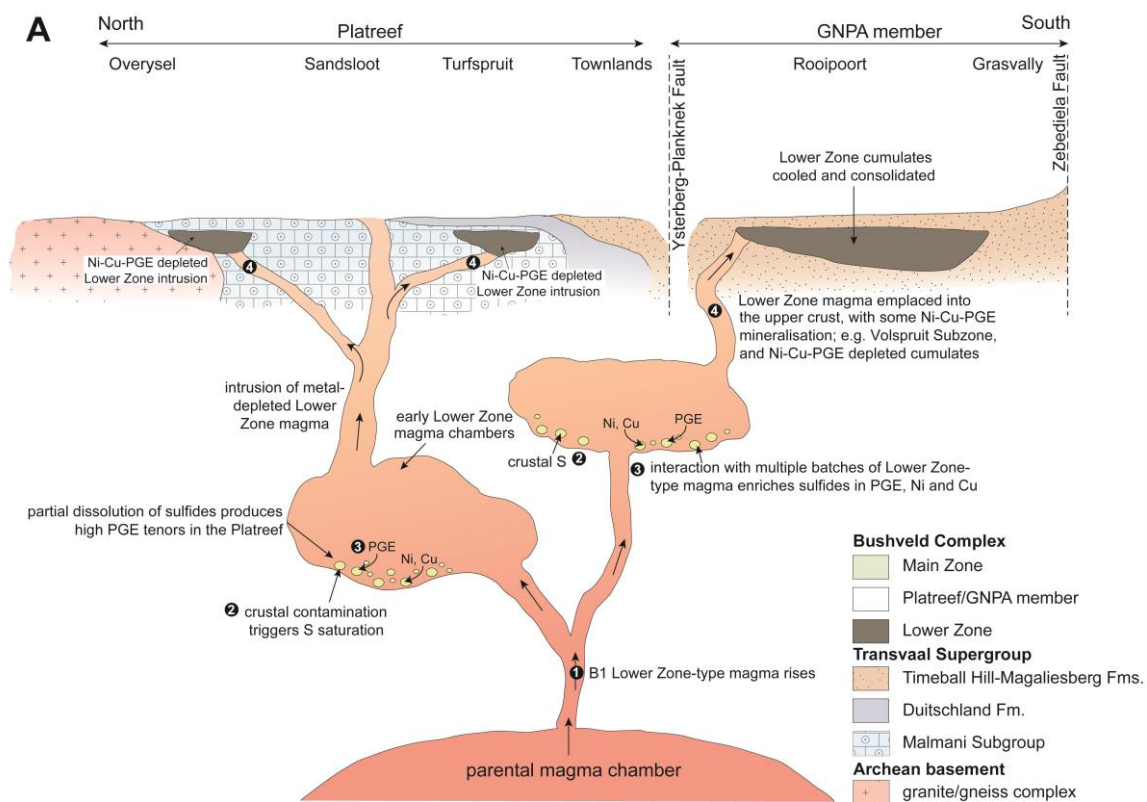
1302

1303 Fig 12

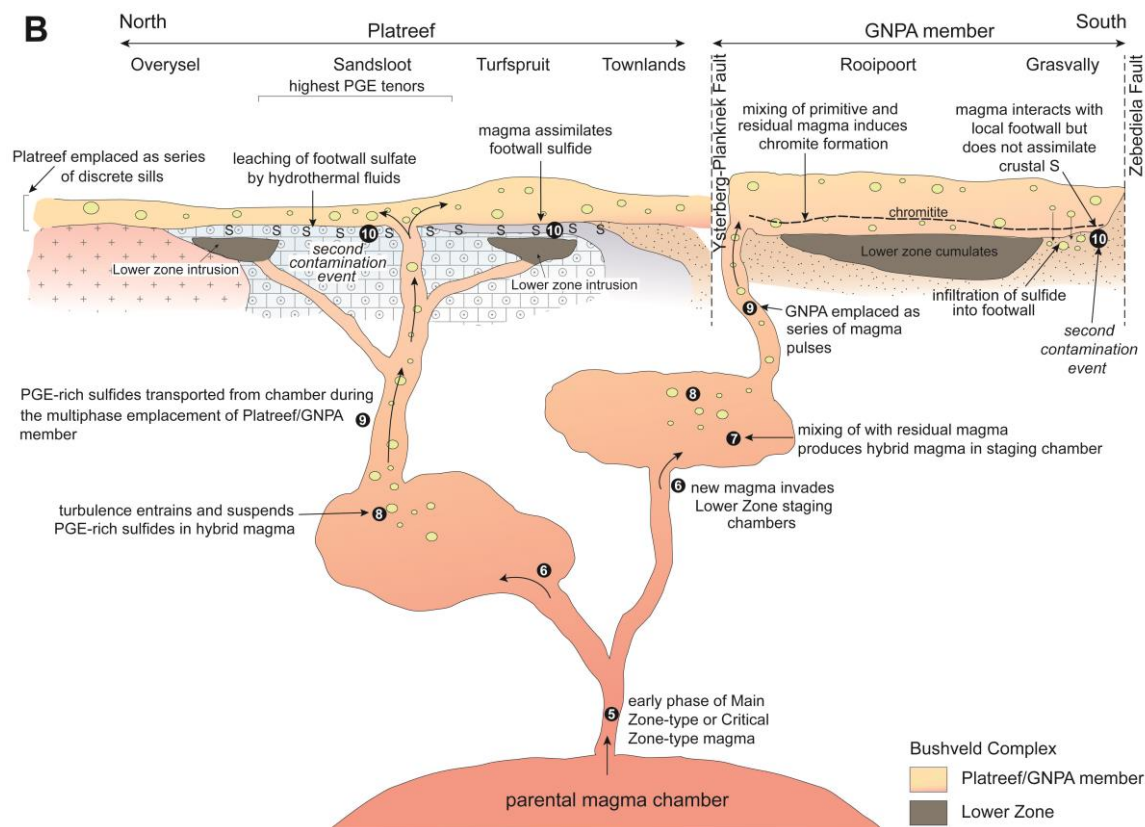


1304

1305



1309 Fig 13B



1310

1311

